

Fault branching and rupture directivity

Sonia Fliss

Laboratoire de Mécanique, Ecole Polytechnique, Palaiseau, France

Harsha S. Bhat

Division of Engineering and Applied Sciences, Harvard University, Cambridge, Massachusetts, USA

Renata Dmowska and James R. Rice

Department of Earth and Planetary Sciences and Division of Engineering and Applied Sciences, Harvard University, Cambridge, Massachusetts, USA

Received 8 August 2004; revised 10 January 2005; accepted 2 March 2005; published 29 June 2005.

[1] Could the directivity of a complex earthquake be inferred from the ruptured fault branches it created? Typically, branches develop in forward orientation, making acute angles relative to the propagation direction. Direct backward branching of the same style as the main rupture (e.g., both right lateral) is disallowed by the stress field at the rupture front. Here we propose another mechanism of backward branching. In that mechanism, rupture stops along one fault strand, radiates stress to a neighboring strand, nucleates there, and develops bilaterally, generating a backward branch. Such makes diagnosing directivity of a past earthquake difficult without detailed knowledge of the branching process. As a field example, in the Landers 1992 earthquake, rupture stopped at the northern end of the Kickapoo fault, jumped onto the Homestead Valley fault, and developed bilaterally there, NNW to continue the main rupture but also SSE for 4 km forming a backward branch. We develop theoretical principles underlying such rupture transitions, partly from elastostatic stress analysis, and then simulate the Landers example numerically using a two-dimensional elastodynamic boundary integral equation formulation incorporating slip-weakening rupture. This reproduces the proposed backward branching mechanism based on realistic if simplified fault geometries, prestress orientation corresponding to the region, standard lab friction values for peak strength, and fracture energies characteristic of the Landers event. We also show that the seismic *S* ratio controls the jumpable distance and that curving of a fault toward its compressional side, like locally along the southeastern Homestead Valley fault, induces near-tip increase of compressive normal stress that slows rupture propagation.

Citation: Fliss, S., H. S. Bhat, R. Dmowska, and J. R. Rice (2005), Fault branching and rupture directivity, *J. Geophys. Res.*, 110, B06312, doi:10.1029/2004JB003368.

1. Introduction

[2] The rupture zones of major earthquakes often involve geometric complexities including fault bends, branches and step overs. Recently, some understanding of the mechanics underlying dynamic processes of fault branching and jumping has started to emerge. A new question has emerged as well: Is it possible to judge the directivity of a large earthquake from the rupture pattern it left? The answer to that question would be very useful for risk assessment of future earthquakes, even if it is currently unknown if large earthquakes do systematically repeat their rupture direction (while not necessarily the entire rupture pattern). Here we address a particular, narrower version of that question, namely: Could we

associate the directivity of a major earthquake with the pattern of branches that it left?

[3] That question has been posed by Nakata *et al.* [1998], who proposed to relate the observed surface branching of fault systems with directivity. Their work assumed that all branches were through acute angles in the direction of rupture propagation. However, Dmowska *et al.* [2002] pointed out that for at least some field observations, the rupture paths seemed to branch through highly obtuse angles, as if to propagate “backward” along the branch. In general, there are no observational proofs that this is what really happened in these cases. It is even possible that some obtuse branches are due to early aftershocks. However, in the case examined here involving a particular backward branch in the 1992 Landers, California, earthquake, Poliakov *et al.* [2002] showed that the pattern of damage to a single side of the fault clearly indicates such a backward direction of propagation on that branch. Here we analyze

and numerically simulate the mechanics of such backward branching and relate the results to understanding rupture directivity.

1.1. Diagnosing Rupture Directivity

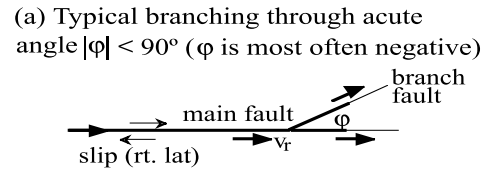
[4] The basic mechanical questions when relating fault branching to rupture directivity are summarized in Figure 1. Figure 1a presents the typical fault branching through acute angle, readily observed in the field and recently analyzed by *Poliakov et al.* [2002] and *Kame et al.* [2003]. The propensity of the fault to branch in that way depends on the orientation of the local prestress field relative to that of the main fault, the rupture velocity at branching junction and the geometry of the branch (the angle between the main and branching faults). The turn of rupture path through an obtuse angle while continuing on main fault is illustrated in Figure 1b and is never favored by the stress field; see section 1.3. What is proposed here as the mechanism of creation of a backward branch is presented in Figure 1c and consists of arrest of rupture propagation along an initial fault strand, radiating stress increase and hence jump of the rupture to a subsidiary fault [Harris et al., 1991; Harris and Day, 1993] on which it nucleates and then propagates bilaterally. Part of the rupture along the neighboring fault creates the backward branch.

[5] Figure 1d presents the mechanical dilemma of backward branching: Did the rupture arrive from the right and branch through an acute angle, as illustrated in Figure 1d (top)? Or, did it arrive from the left, stop, jump, and nucleate on a neighboring fault, then develop bilaterally, as illustrated in Figure 1d (bottom)? The jump here is exaggerated, in real field cases the observation of surface ruptures might not at once provide the right answer. The purpose of the present paper is to document a field example of the latter case as well as to develop theoretical understanding and numerical simulation of the process.

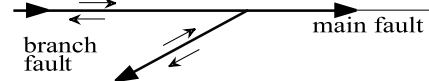
1.2. Field Examples of Backward Branching

[6] We study the transition of the rupture path from the Kickapoo to the Homestead Valley faults, Figure 2, during the 1992 Landers earthquake, so as to leave a backward branch in the rupture path along the southern end of Homestead Valley fault. The rupture started to the SSE of the area covered by the map, along the Johnson Valley fault, and continued far to the NNW, first along the Homestead Valley fault and then the Emerson and Camp Rock faults [Rockwell et al., 2000; Sowers et al., 1994; Spotila and Sieh, 1995; Zachariasen and Sieh, 1995].

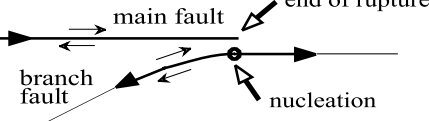
[7] In the 1992 Landers earthquake [Sowers et al., 1994], right-lateral slip on the Johnson Valley Fault propagated first along that fault but then, after several aborted attempts signaled by the short surface breaks shown, it branched to the dilatational side onto the Kickapoo fault, at an angle $\varphi \approx -30^\circ$. The rupture also continued a few kilometers to the NNW on the main (Johnson Valley) fault. That exemplifies the type of branching typically considered, through an acute angle relative to the direction of propagation along the primary fault. (The Johnson Valley and Kickapoo branch has been analyzed as a field case in support of recent theoretical work [Poliakov et al., 2002; Kame et al., 2003], explaining how such typical branching depends on



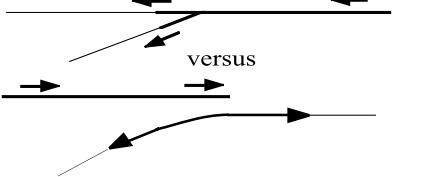
(a) Typical branching through acute angle $|\varphi| < 90^\circ$ (φ is most often negative)



(b) Turn of rupture path through obtuse φ angle while continuing on main fault (never favored by stress field)



(c) Jumping mechanism; nucleation of bilateral rupture on a neighboring fault



(d) Given the branch geometry, what was the direction of rupture propagation?

prestress state, branch geometry, and rupture propagation speed as the branch junction is approached.)

[8] What is of interest here, however, is that the rupture, after propagating along the Kickapoo segment, transitioned to the Homestead Valley fault and progressed not just to the north on that fault, in continuation of the main Landers rupture, but also backward along the Homestead Valley fault where it curves to the SSE. That forms the backward branch (backward relative to the main direction of rupture propagation) that we consider, a prominent feature of 4 km length. Measurements of surface slip along that backward branch [Sowers et al., 1994] show right-lateral slip, decreasing toward the SSE. Prominent surface breaks were also observed along the western side of the Homestead Valley fault (Figure 2). From those it can be argued [Poliakov et al., 2002; Kame et al., 2003] that given the local principal prestress orientation [Hardebeck and Hauksson, 2001], the western side of the southern Homestead Valley fault should have been the dilatational side of the rupture. That, along with the slip pattern, suggests that rupture initiated on the Homestead Valley fault in the region where it is closely approached by the Kickapoo fault, near the northern termination of the latter, and then propagated bilaterally, both north and SSE along the Homestead Valley fault.

[9] The following are other cases, also from the Eastern California Shear Zone, of rupture transitions that leave backward branched rupture patterns: As rupture continued along the Homestead Valley fault, NNW of the region

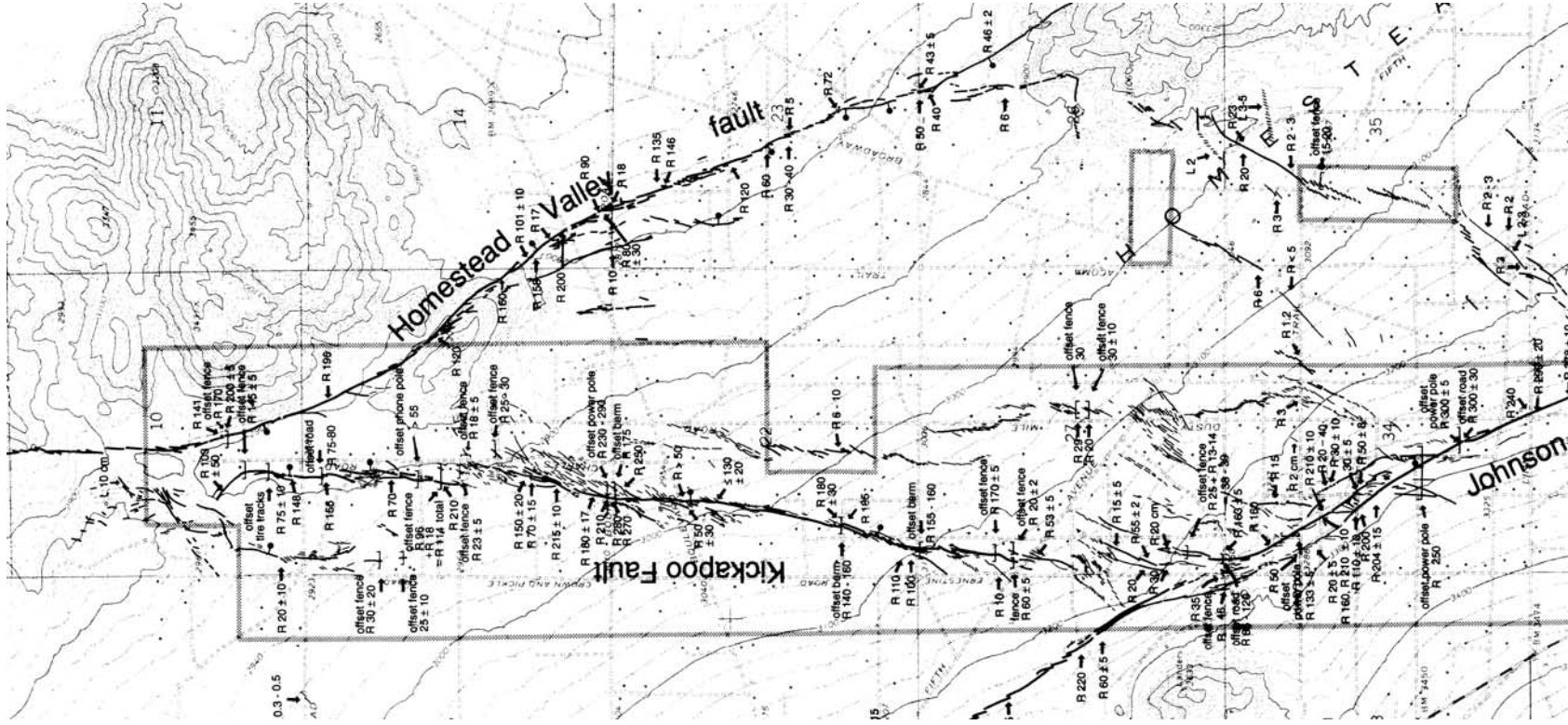


Figure 2. Map from Sowers *et al.* [1994] showing region of transition from the Johnson Valley to the Kickapoo and to the Homestead Valley faults during the 1992 Landers earthquake. The thickest lines show fault breaks with surface slip >1 m, intermediate lines >0.05 m, and thinnest lines >0.01 m.

mapped in Figure 2, there was a transition of the rupture path to the Emerson fault, but while primarily propagating to the NW, the rupture also progressed backward along different SSE splays of the Emerson fault [Zachariasen and Sieh, 1995]. The rupture path next transitioned from the Emerson to the Camp Rock fault, and in doing so again generated a backward branch to the SSE on the Camp Rock fault. Another case is in the 1999 Hector Mine earthquake. Rupture originated on a buried fault without surface trace [Li *et al.*, 2002; Hauksson *et al.*, 2002; Oglesby *et al.*, 2003a] and progressed bilaterally south and north. In the south it met the Lavic Lake fault and progressed a large distance south on it but also progressed backward, i.e., NNW, along the northern stretch of the Lavic Lake fault. The angle between the buried fault and the northern Lavic Lake fault is $\varphi \approx -160^\circ$, and that NNW stretch extends around 15 km, defining a major backward branch.

1.3. Backward Branching Mechanisms

[10] Such examples with highly obtuse branch angles (backward branching) suggest that there may be no simple correlation between fault geometry and directivity. An important question is whether those obtuse branches actually involved a rupture path which directly turned through an obtuse angle (while continuing also on the main fault) like in Figure 1b, or rather involved arrest by a barrier on the original fault and jumping to a neighboring fault, on which rupture propagated bilaterally (Figure 1c). The importance of stopping on the main fault to making the jumping mechanism possible will be discussed later.

[11] Stress fields around a dynamically moving mode II crack tip with right-lateral slip have been reported by Poliakov *et al.* [2002]. At the obtuse angles considered, they predict strongly left-lateral shear stress and hence are inconsistent with having the rupture path directly turn through highly obtuse angles like in Figure 1b if slip is to remain right lateral on the branch. Thus we discount that mechanism. Note that there is no inhibition to obtuse angle branching with left-lateral slip on the branch; that situation was observed in lab experiments under impact loading [Rousseau and Rosakis, 2003]. Rousseau and Rosakis diagnosed small tensile fracture arrays along the extensional side of the rupture where the slip was right versus left lateral.

[12] On the other hand, there is evidence that the Kickapoo and Homestead Valley faults are disjoint from one another, so that the transition fits the stopping and jumping scenario of Figure 1c. First, mapping of observable fault slip (>10 mm) in the vicinity of the transition [Sowers *et al.*, 1994] (see Figure 2) suggests that the faults do not actually intersect one another at the surface. Second, Li *et al.* [1994] used studies of fault zone trapped waves to show that there was transmission in a channel along the southern Johnson Valley and Kickapoo faults and in another channel along the Homestead Valley fault but no communication between those channels. Those results suggest that the Kickapoo and Homestead Valley faults do not join, at least at the possibly shallow depths controlling the observations. Finally, precise relative relocations of Landers aftershocks have been used to image the fault strands at depth [Felzer and Beroza,

1999] and suggest that they form two discrete structures throughout the seismogenic depth range.

1.4. Branching and Rupture Directivity

[13] If such a jumping mechanism turns out to be a reasonably general mechanism of backward branching, then an implication for the Nakata *et al.* [1998] aim of inferring rupture directivity from branch geometry is that such will be possible only when rather detailed characterization of fault connectivity (by surface geology, microearthquakes relocation, trapped waves) can be carried out in the vicinity of the branching junction. Such studies must ascertain whether direct turning of the rupture path through an angle, or jumping and then propagating bilaterally, were involved in prior events. Those two possibilities have opposite implications (Figure 1d) for how to associate directivity with a (nominally) branched fault geometry.

[14] In the following sections of the paper, we analyze the mechanics of rupture propagation and slip transfer for faults with complex geometries similar to those near the Kickapoo to Homestead Valley transition. We show that these considerations strongly support the possibility that the backward branch formed by the jumping and bilateral propagation mechanism of Figure 1c. (Further, we note that Aochi and Fukuyama [2002] tried to simulate the Kickapoo to Homestead Valley rupture transition by assuming that the faults were actually connected in an inverted “y” type of branch junction, rather than forming the step over configuration that we assume here. They could then achieve rupture continuation from Kickapoo onto the northern Homestead Valley fault, but not onto the southeastern part of the Homestead Valley fault which is the object of our study here, and which hosted the backward branch of rupture observed.)

2. Choice of Prestress and Modeling Parameters

2.1. Parameters

[15] For convenience, we treat the Kickapoo fault near its northern termination as being straight and coincident with the x axis, which runs south to north (like the fault itself does approximately in that region; Figure 2). The fault plane is $y = 0$, with the y axis positive to the west, and we perform two-dimensional (2-D) modeling in that x, y plane. Here and later, all faults are considered to undergo right-lateral strike slip.

[16] The prestress, i.e., the tectonic stress in the region, has the form

$$\sigma_{ij}^0 = \begin{pmatrix} \sigma_{xx}^0 & \sigma_{xy}^0 \\ \sigma_{yx}^0 & \sigma_{yy}^0 \end{pmatrix} \quad (1)$$

as regards in-plane components, where normal stresses are positive if tensile. We should actually think of these as effective stresses $(\sigma_{ij}^0)^{\text{tot}} + p^0 \delta_{ij}$, where p^0 denotes initial fluid pore pressure. As in the work by Kame *et al.* [2003], in which the branching from the Johnson Valley to Kickapoo faults during this earthquake was studied, the static friction coefficient $\tan(\Phi_s) = \mu_s$ is taken as 0.6, generally consistent with laboratory values, and cohesion is neglected. It is less clear what to take for the dynamic coefficient $\tan(\Phi_d) = \mu_d$ after slip weakening, or how reasonable it is to regard it as

actually constant at large earthquake slip, especially when thermal weakening and possible fluidization is considered. Values of $\mu_d/\mu_s = 0.8$ and 0.2 have been tested and the results do not show significant differences. Only the results for $\mu_d/\mu_s = 0.2$ will be shown here. We choose the shear modulus $\mu = 30$ GPa and the Poisson ratio $\nu = 0.25$ ($\lambda = \mu$).

[17] Most of our results can be expressed in nondimensional form but when necessary for numerical illustrations here, we have used $G = 1$ MJ/m² for the crack energy release rate and $\sigma_{yy}^0 = -50$ MPa. For the corresponding σ_{xx}^0 , to be discussed subsequently, the in-plane invariant $(\sigma_{xx}^0 + \sigma_{yy}^0)/2 = -59.5$ MPa. Assuming ideal strike-slip rupture (i.e., vanishing intermediate deviatoric stress), that invariant is equal to the effective overburden, and assuming hydrostatic pore pressure, that corresponds to a depth of 3.3 km. Given the nondimensionalization of our problem, features of the solution such as the speed of rupture propagation and its time evolution, and details of if, where and how slip transfers between faults, would be unchanged for the choice of parameters $G = 4$ MJ/m² and $\sigma_{yy}^0 = -100$ MPa. That change, which keeps the slip-weakening zone length R at the same (time-dependent) size throughout the rupture as for the above case, would correspond to a depth of 6.6 km. Such depth is a reasonable estimate of the centroidal depth of rupture during the Landers event, and the fracture energy is close to the 5 MJ/m² inferred for it by seismic slip inversions, fitted to 3-D analyses of slip-weakening rupture [Olsen et al., 1997; Peyrat et al., 2001].

[18] To properly determine the in-plane prestress field around the faults, if all the stresses are normalized by $-\sigma_{yy}^0$, two further quantities have to be specified. First, on the basis of inference of principal stress directions from microseismicity by *Hardebeck and Hauksson* [2001], the maximum principal compressive stress direction around the faults is approximately 30° east of north. Because the tangent direction to the Kickapoo fault is about north. Thus there is an angle $\Psi \approx 30^\circ$ between the most compressive stress and that fault (Figure 3).

[19] We have to specify one more value, for example the shear stress ratio, $\sigma_{yx}^0/(-\sigma_{yy}^0)$. There is no rigorous way to specify that. We choose it according to considerations of rupture propagation velocity v_r . Supershear v_r is sometimes, but only relatively rarely, inferred for natural events. Thus we choose parameters so that v_r remains sub-Rayleigh. *Andrews* [1976] shows the influence on v_r of the ratio

$$S = (\tau_p - \sigma_{yx}^0) / (\sigma_{yx}^0 - \tau_r) \quad (2)$$

where $\tau_p = -\mu_s \sigma_{yy}^0$ is the peak strength and $\tau_r = -\mu_d \sigma_{yy}^0$ is the residual strength after slip weakening. When S is small enough, a transition from sub-Rayleigh to supershear propagation will occur, so we do not want S to be so small as to allow that in our modeling. However, in a simple static study to follow, we show that the smaller is the value of S , the larger is the maximum distance that can be jumped, and vice versa. So it won't do to make S too large, and a compromise has to be reached. Using Figure 9 of *Andrews* [1976] (which shows the v_r achieved as a function of S and the ratio of the length L of the ruptured zone to the minimum unstable crack length L_c), and the static study, we have chosen $S = 1.3$. For that, v_r remains sub-Rayleigh in our configuration. It leads to $\sigma_{yx}^0/(-\sigma_{yy}^0) = 0.33$.

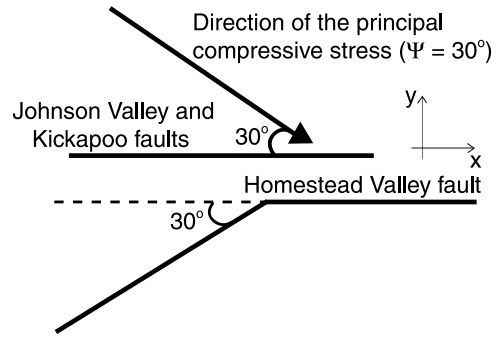


Figure 3. Simple modeling of the faults involved in the 1992 Landers earthquake.

[20] Given the principal direction at $\Psi = 30^\circ$, we can then calculate, the remaining in-plane stress ratio as $\sigma_{yx}^0/(-\sigma_{yy}^0) = 1.38$. That corresponds to the in-plane invariant $(\sigma_{xx}^0 + \sigma_{yy}^0)/2 = 1.19\sigma_{yy}^0$.

2.2. Strength Constraints on Prestress

[21] In order to make the prestress field realistic we have to satisfy some mechanical conditions. Since large regions of earth cannot sustain tensile stresses, no principal stress should be tensile. Also, the prestress field should not violate the Mohr-Coulomb criterion for onset of frictional rupture.

[22] With the two parameters, Ψ and $\sigma_{yx}^0/(-\sigma_{yy}^0)$, the condition to avoid tension is:

$$\frac{\sigma_{yx}^0}{-\sigma_{yy}^0} \tan(\Psi) < 1 \quad (3)$$

which is respected with our parameters. Second, to make sure that the prestress does not violate the Coulomb failure condition, i.e., that $|\sigma_{21}^0| < -\mu_s \sigma_{22}^0$, for any orientation of the faults (Figure 4), $\sigma_{yx}^0/(-\sigma_{yy}^0)$ has to satisfy

$$\frac{\sigma_{yx}^0}{-\sigma_{yy}^0} < \frac{\sin(\Phi_s) \sin(2\Psi)}{1 - \sin(\Phi_s) \cos(2\Psi)} \quad (4)$$

In this case, the condition is $\sigma_{yx}^0/(-\sigma_{yy}^0) < 0.60$ which is also respected.

3. Elastostatic Singular Crack Modeling

[23] The goal of this section is to give a general idea of stressing near the end of an arrested rupture, to begin to determine conditions so that a rupture can jump to another fault, parallel [Harris and Day, 1993] or not. For simplicity, we start with the study of an elastostatic singular crack model of a mode II rupture.

[24] We suppose that the two ends of a finite rupture have finished their motion and that all along the crack there is sustained a stress equal to the residual shear strength, $\sigma_{yx} = \tau_r = -\mu_d \sigma_{yy}^0$ (as represented in Figure 5). This static study can be understood as a study after the motion. It is suggestive only, because we cannot preclude the possibility that dynamic stresses very close to the stopped rupture tip were higher than in the final static field; they cannot be on the crack plane itself, from basic results on unsteady crack dynamics [Fossum and Freund, 1975], but the situation is

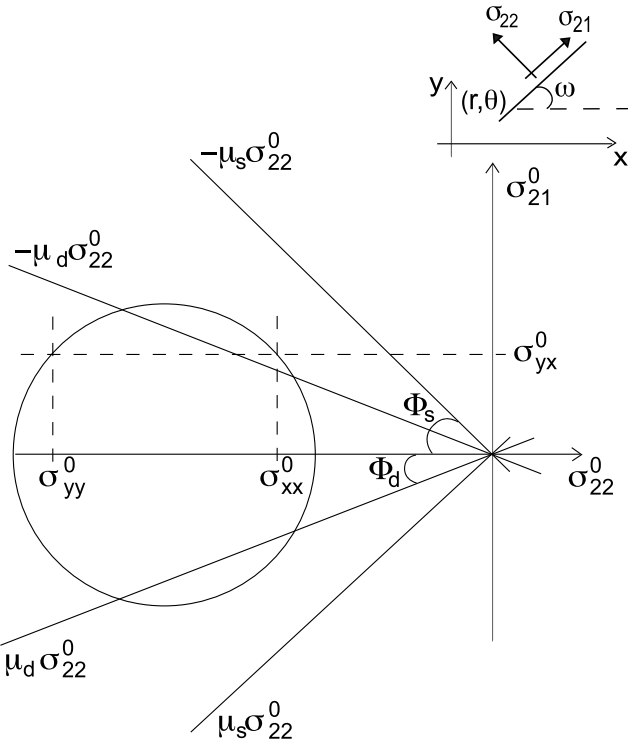


Figure 4. Mohr circle of the prestress. Conditions required to not violate the failure conditions in any orientation and to favor the propagation of the rupture for some orientations.

more complex in the near tip field at other orientations relative to the rupture, as well as at more distant locations.

3.1. Faults

[25] In the branching transition from the Johnson Valley to the Kickapoo faults, we will neglect the few km continuation along the former, and consider it and the Kickapoo fault as one, and only one, main fault, whose length is 15 km. (Of course the actual length is longer, but we do not want to allow crack lengths in a 2-D model which are much greater than the seismogenic thickness of the crust. From 3-D considerations that thickness sets a limit, which is not contained in 2-D models, on how much further increase of crack length along strike can increase the stress concentration at the crack ends.) To determine the stress distribution due to the crack for the singular static model, the Johnson Valley and Kickapoo faults are represented, just here but not in the elastodynamic study to follow, as a straight fault of 15 km length. Figure 3 gives one simple modeling of the faults, with the Homestead Valley fault at orientation angles $\omega = 0^\circ$ and 30° , in pieces, relative to the straight fault. Actually, the smallest distance between the Kickapoo and Homestead Valley fault is a few hundred meters (between 200 and 300 m) [Sowers *et al.*, 1994], and the orientation angle ω of the closest parts of the latter fault, relative to Kickapoo is between 0° and 10° .

3.2. Static Stress Distribution

[26] Consider a single straight crack extending from $x = -X$ to 0 on the x axis, with $X = 15$ km, in the infinite x, y plane, in a mode II configuration. We study the stress distribution near the crack tip $x = 0$. As explained by Rice

[1980] and Poliakov *et al.* [2002], the final stress σ_{ij} is the sum of the initial stress σ_{ij}^0 and stress change $\Delta\sigma_{ij}$ due to introduction of the crack, and is given by

$$\sigma_{ij} = \frac{K_{II}}{\sqrt{2\pi r}} \Sigma_{ij}(\theta) + \begin{pmatrix} \sigma_{xx}^0 & \tau_r \\ \tau_r & \sigma_{yy}^0 \end{pmatrix} + O(\sqrt{r}) \quad (5)$$

where (r, θ) are the polar coordinates (the origin is the crack tip), the $\Sigma_{ij}(\theta)$ are certain universal functions normalized to $\Sigma_{yx}(0) = 1$ (see, e.g., *Lawn and Wilshaw* [1993] or *Rice* [1968] or other sources on elastic crack theory) and $\tau_r = -\mu_d \sigma_{yy}^0$ the residual shear strength. In the present case the stress intensity factor is

$$K_{II} = \left(\sigma_{xy}^0 - \tau_r \right) \sqrt{\pi X/2} \quad (6)$$

and $O(\sqrt{r})$ denotes term which vanish in proportion to \sqrt{r} or faster as $r \rightarrow 0$.

[27] The full representation of the stress field, effectively identifying explicitly all terms in equation (5) including those denoted $O(\sqrt{r})$, may be done using standard techniques in the 2-D elasticity analysis of cracked solids [e.g., *Rice*, 1968] to solve for $\Delta\sigma_{ij}$. Thus letting the complex position be denoted by $z = X/2 + x + iy$,

$$\begin{aligned} \sigma_{xx} + \sigma_{yy} &= \sigma_{xx}^0 + \sigma_{yy}^0 + 4\text{Re}[\phi'(z)] \\ \sigma_{yy} - \sigma_{xx} + 2i\sigma_{yx} &= \sigma_{yy}^0 - \sigma_{xx}^0 + 2i\sigma_{yx}^0 + 2[\bar{z}\phi''(z) + \psi'(z)] \end{aligned} \quad (7)$$

where for our mode II problem

$$\phi'(z) = \frac{\sigma_{yy}^0 - \tau_r}{2i} \left[\frac{z}{(z^2 - X^2/4)^{1/2}} - 1 \right], \quad \psi'(z) = -2\phi'(z) - z\phi''(z) \quad (8)$$

[28] Representation of the stress field for purposes of our plots in Figure 6 is done using the full equations (7) and (8), although the plots are very similar in appearance when we use equation (5) and simply neglect the terms denoted $O(\sqrt{r})$.

3.3. Conditions for Rupture Nucleation on a Nearby Fault

[29] In the Coulomb friction model, rupture can nucleate at any point if the shear stress is higher than the static

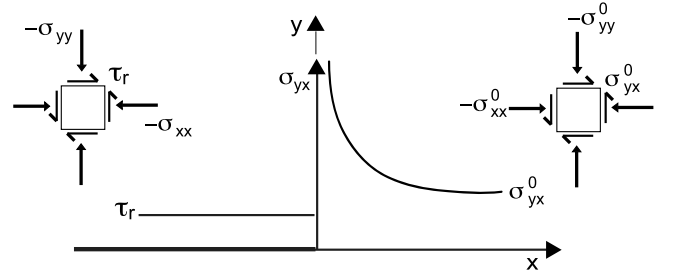


Figure 5. Singular elastic crack model (mode II shear) for static rupture. Stress state shown (left) behind the tip, near the fault surface, and (right) far ahead, where it coincides with the prestress.

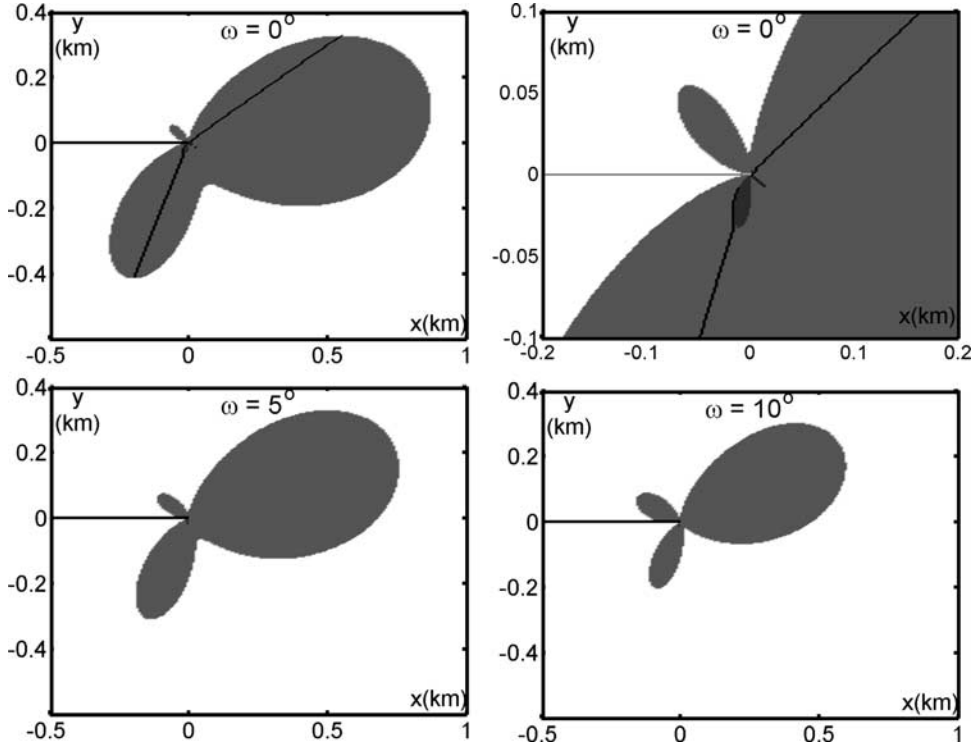


Figure 6. Areas where nucleation of a rupture is possible, for various orientation angles ω of the second fault. Angles $\omega = 0^\circ, 5^\circ$ and 10° , are chosen with reference to the geometry of the Homestead Valley fault. The medium gray regions are those for which $\sigma_{\text{coul}} = \sigma_{21} + \mu_s \sigma_{22} > 0$ on a fault trace with orientation ω (i.e., areas where right-lateral failure nucleation is possible). Small, dark gray regions near the crack tip are areas where the elastically calculated normal stress on the second fault is tensile ($\sigma_{22} > 0$); see enlarged view of region, for the $\omega = 0^\circ$ case, in top right. The black lines in the upper two panels, for the $\omega = 0^\circ$ case, represent the points where, for each fixed y , σ_{coul} attains its maximum with respect to x .

friction strength. So, it is relevant to consider the normal and shear stresses (σ_{22}, σ_{21}) at a point on a potential fault, whose polar coordinates are (r, θ) . Different orientation angles ω given to the second fault are analyzed, and different situations of nucleation may arise as follows:

[30] 1. If $\sigma_{22} < 0$ and $\sigma_{21} > \mu_s(-\sigma_{22})$, right-lateral slip nucleates. The area where this condition is met is represented in medium gray.

[31] 2. If $\sigma_{22} < 0$ and $\sigma_{21} < -\mu_s(-\sigma_{22})$, left-lateral slip nucleates. The area where the condition is met is represented in light gray. In fact, we'll find none such for our ω range studied.

[32] 3. If $\sigma_{22} > 0$, the area is represented in dark gray. Compressional remote stress fields only are studied so that the faults remained closed but it is interesting to test if there are local areas where the normal stress is predicted to be extensional.

[33] With these different representations, we analyze where a nearby nucleation on a second fault could occur, at least as based on the static field. This allows a preliminary estimate of the influence of different parameters: characteristics of the step over (width and overlap of the second fault, its local orientation ω), prestress, stress drop $\sigma_{yx}^0 - \tau_r$, and ratio $S = (\tau_p - \sigma_{yx}^0)/(\sigma_{yx}^0 - \tau_r)$.

3.4. Results for Some Second-Fault Orientations

[34] Results based on our model parameters as in sections 2 and 3.1 are shown in Figure 6 for local $\omega =$

$0^\circ, 5^\circ$ and 10° . We see that this simple static analysis is consistent with some conclusions of the *Harris and Day* [1993] dynamic study of step overs between parallel fault strands (case $\omega = 0^\circ$). First is the difference between the compressional and the dilational sides. Indeed, there is no symmetry, and the areas of possible nucleation and the maximum “jumpable” distance are very different according to the overlap.

[35] Moreover, for these orientations only right-lateral slip is possible; there are no light gray regions signaling left-lateral slip. The higher is the orientation of the second fault the smaller are the maximum jumpable distance and the area where the nucleation is possible.

[36] There are very small regions adjoining the crack tip on the dilational side where the normal stress is positive, signaled by dark gray shading. That means a possible opening of the secondary fault, but strong conclusions cannot be drawn because this is particularly near the crack tip (where the simple model adopted has a singularity of the stress), and also because we have not analyzed effects on the stress field of plastic yielding in the Coulomb failure regions shown to envelop those zones.

[37] Comparing the stress distribution calculations for several orientations which represent where the nucleation of a rupture is possible, given the position of the curved Homestead Valley fault and its orientations, we can anticipate that the rupture should jump from Kickapoo fault and might nucleate in several positions along the Homestead

Valley fault, Figure 6, although this analysis cannot tell us which one will nucleate first.

3.5. Some Analytical Results

[38] We can use our representation of the stress field to make simple estimates of the maximally stressed offset location (x coordinate) for a given step over width (y coordinate), and of the scaling of maximum vulnerable width with other parameters, especially S . First note that Figure 6 (top) correspond to the case of two parallel faults ($\omega = 0^\circ$). They show that the loci of maximal Coulomb stress $\sigma_{\text{coul}} = \sigma_{21}^0 + \mu_s \sigma_{22}^0$, for various y , define a pair of nearly straight lines emanating from the crack tip. Considering points where the normal stress is compressive and the slip is right lateral, that geometry and other features of the stressing can be understood when stresses are written like in equation (5), and we neglect the $O(\sqrt{r})$ terms to simplify (as commented in section 3.2, they have little effect on the shapes shown in Figure 6). Using x, y variables instead of r, θ , equation (5) leads to

$$\sigma_{\text{coul}} = (\sigma_{21}^0 + \mu_s \sigma_{22}^0) + \left[\sqrt{\frac{X}{|y|}} F\left(\frac{x}{y}\right) + C \right] (\sigma_{yx}^0 + \mu_d \sigma_{yy}^0) \quad (9)$$

Here the first pair of terms give the Coulomb prestress; they are dependent on ω and are linear in the σ_{ij}^0 . In the remaining terms $F(x/y)$ is a dimensionless function proportional to $\sqrt{|\sin(\theta)|} [\Sigma_{21}(\theta) + \mu_s \Sigma_{22}(\theta)]$ and having different forms in $y > 0$ and $y < 0$, whereas C is a constant; both F and C depend on ω and vary linearly with μ_s .

[39] That expression makes it clear that σ_{coul} is maximum relative to x , at any given y , when F is a maximum relative to its dimensionless argument x/y . That defines loci $x/y = \text{constant}$ in $y > 0$ and $y < 0$, thus predicting that the heavy lines in Figure 6 (top) should be precisely straight, to the neglect of the $O(\sqrt{r})$ terms in equation (5). As noted, they are indeed nearly straight, when we include all terms like in equations (7) and (8).

[40] Finally, for the $\omega = 0^\circ$ case of parallel faults [Harris and Day, 1993] we can estimate the influence of the S ratio on the maximum jumpable distance H_{max} . Writing $\tau_r = -\mu_d \sigma_{yy}^0$ in equation (5) and making C explicit in equation (9) leads to

$$\sigma_{\text{coul}} = (-\mu_d \sigma_{yy}^0 + \mu_s \sigma_{yy}^0) + \sqrt{\frac{X}{|y|}} F\left(\frac{x}{y}\right) (\sigma_{yx}^0 + \mu_d \sigma_{yy}^0) \quad (10)$$

where $F(x/y)$ is linear in μ_s . Identifying the terms corresponding to τ_p and τ_r , and setting the argument x/y of F to correspond to the maximal value, say $F_m (> 0$, but different on the two sides of the fault), and using the definition of S , this becomes

$$\frac{\sigma_{\text{coul}}}{\sigma_{yx}^0 - \tau_r} = F_m \sqrt{\frac{X}{|y|}} - (1 + S) \quad (11)$$

Hence the maximum jumpable distance H_{max} is the largest value of $|y|$ for which the right side is positive, and that yields

$$\frac{H_{\text{max}}}{X} = \left(\frac{F_m}{1 + S} \right)^2 = F_m^2 \left(\frac{\sigma_{yx}^0 - \tau_r}{\tau_p - \tau_r} \right)^2 \quad (12)$$

in which the coefficient of proportionality (F_m^2) depends on μ_s . Thus H_{max} increases when S decreases (i.e., when prestress σ_{yx}^0 is larger); Figure 6 is for $S = 1.3$ but the results can thereby be scaled to other S .

3.6. Long-Range Dynamic Rupture Propagation

[41] If the rupture has nucleated along a suitable direction, will the prestress be consistent with an arbitrary amount of propagation along that direction? This condition will be met for at least some orientations if some part of the Mohr Circle lies outside the wedge of angle $2\Phi_d$, as represented in Figure 4.

[42] Typically, $\sigma_{yx}^0 / (-\sigma_{yy}^0) > \mu_d$ makes long-range dynamic rupture possible along the part of Homestead Valley fault parallel to the x axis. The condition to make it possible along the other part of the fault, with a maximum misorientation $\omega = 30^\circ$, is that $\sigma_{12}^0 > -\mu_d \sigma_{22}^0$, which is satisfied if $\sigma_{yx}^0 / (-\sigma_{yy}^0) > 0.122$.

[43] Thus the prestress field allows dynamic rupture along the Homestead Valley fault. Such has been inferred, to the N and at least for about 4 km to the SSE, in the earthquake.

[44] From this simple static analysis, we have guidelines for knowing if a fault is near enough to the tip of another one for slip to be nucleated. However, we do not know if the rupture can propagate and if it does so bilaterally. A dynamic study is required, and that analysis follows. It includes the time dependence of fault rupture, stress waves, and time-dependent stress concentrations generated during the rupture process (e.g., we will show important dynamic normal stress changes on curved parts of the fault along which ω is changing).

4. Elastodynamic Slip-Weakening Rupture Modeling

4.1. Geometric Modeling of the Faults

[45] We again choose the x axis parallel to the northern part of the Kickapoo fault, treating its last 4 km as straight. We do not consider the short rupture along the Johnson Valley fault north of its branch with Kickapoo, and treat that pair of faults as a single fault, curved before reaching the straight Kickapoo segment. Because the 2-D model is not sensible for crack lengths greater than the seismogenic thickness of the crust, we have to reduce the rupturing length of the Johnson Valley fault to 10 km, but we keep the actual length of the Kickapoo fault, about 5 km. The angle φ between the two faults is $\sim 30^\circ$. The origin of the x, y system is taken at the beginning of the straight part of the Kickapoo fault. That is also the origin for the curvilinear distance s along the fault, so that $s > 0$ on the 4 km straight part. The geometrical modeling is shown in Figure 7 in the x - y plane.

[46] For the boundary integral equation (BIE) numerical analysis, we cover all potentially rupturing faults with uniformly sized cells of length Δs . Our parameter choices allow us to choose $\Delta s = 40$ m (25 cells over 1 km length), and still reasonably meet requirements [Kame et al., 2003] for discretized numerical BIE solutions to suitably represent the continuum limit of the slip-weakening rupture model.

[47] Thus the straight northern segment of the Kickapoo fault has length 4 km = $100\Delta s$. In the $s < 0$ region the Johnson Valley-Kickapoo fault begins to curve progressively

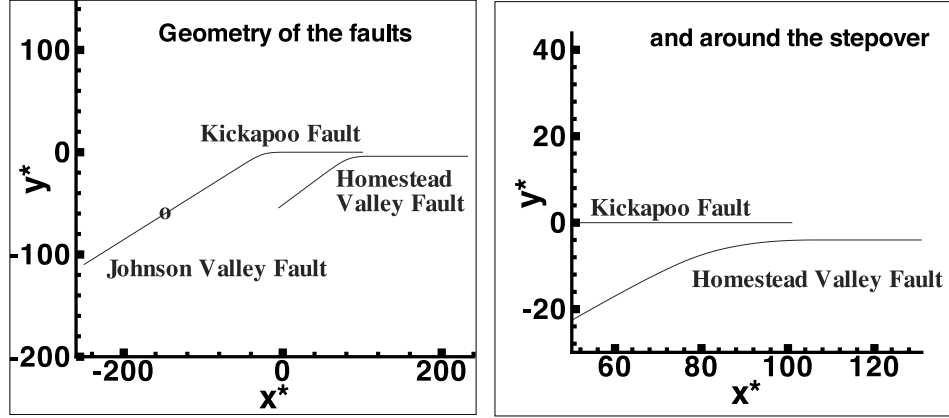


Figure 7. Geometry of faults in the x , y plane, $x^* = 3x/R_0^o$, $y^* = 3y/R_0^o$. The x axis corresponds to the orientation of the portion of the Kickapoo fault that is modeled straight N-S. The orientation of the Johnson Valley fault decreases from 0° to 26° . The orientation of left half of Homestead Valley fault decreases from 0° to 30° .

SSE along 2 km ($50\Delta s$) and then keeps the same orientation at 26° east of south along 9 km ($225\Delta s$).

[48] For the modeling of the Homestead Valley fault, we know that the step over with the Kickapoo fault is between 200 and 300 m at closest approach. From *Sowers et al.* [1994], the backward propagation seems to stop at about 4 km SSE from that closest region. Thus we choose to represent the entire part of the fault modeled with a length of 10 km ($250\Delta s$). Although rupture continues along Homestead Valley well to the north, in our model slip propagation is blocked on it 6 km north of the nucleation. We have verified that all of the action as regards forming the backward branch is over before waves from that artificial northern blockage of rupture propagate back into the region of interest.

[49] The northern terminus of Kickapoo is offset in a direction perpendicular to Kickapoo by 200 m from the Homestead Valley fault. Thus for the simulation, the center of the 10 km long Homestead Valley fault is chosen to be at 160 m east ($y = -4\Delta s$) and 280 m north ($x = 107\Delta s$) of the terminus of Kickapoo. The northern half of the Homestead Valley fault ($125\Delta s$) is straight and parallel to Kickapoo. Along the curved SSE half, the orientation of the fault varies from 0° to 30° along 2 km ($50\Delta s$) to reach the value of 30° and finally keeps it along the last 3 km ($75\Delta s$).

4.2. Slip-Weakening Coulomb Friction Law

[50] In our modeling, the rupture was allowed to propagate spontaneously using a slip-weakening friction law [*Ida*, 1972; *Palmer and Rice*, 1973]. The fault strength τ , once reaching the peak strength τ_p , decreases linearly (in the most commonly adopted variant of slip weakening) with the slip, to the residual strength τ_r , and becomes constant when the slip Δu exceeds an amount D_c , the critical slip. D_c is considered to be a parameter inherent in the rupture process. Moreover, the Coulomb friction concept is added to the slip-weakening law so that τ is proportional to the normal stress $-\sigma_n$ at any particular amount of slip, as in Figure 8. That is,

$$\tau = \tau_r + (\tau_p - \tau_r) \left(1 - \frac{\Delta u}{D_c} \right) H \left(1 - \frac{\Delta u}{D_c} \right) \quad (13)$$

where

$$\tau_p = \mu_s (-\sigma_n) \quad \tau_r = \mu_d (-\sigma_n) \quad (14)$$

[51] This criterion, contrary to the critical stress intensity factor criterion, does not suffer the unphysical infinite stresses at the edges: there is a continuous stress distribution at the crack tip (see Figure 9). The notation R denotes the length of the slip-weakening zone, i.e., the zone in which $0 < \Delta u < D_c$ and $\sigma_{21} > \tau_r$.

[52] *Palmer and Rice* [1973] and *Rice* [1968] showed that if the length of the slip weakening zone, R_0 , of a static crack is small compared to all geometric dimensions of the model, such as overall crack size, then we can estimate from the energy balance of elastic-singular crack theory, with fracture energy G expressed in terms of the slip-weakening law, the minimum nucleation size of an initial crack so that the rupture can propagate. For $\lambda = \mu$ that is

$$L_c = \frac{16}{3\pi} \frac{\mu G}{(\sigma_{xy}^0 - \tau_r)^2} = \frac{8}{3\pi} \frac{\mu(\tau_p - \tau_r)}{(\sigma_{xy}^0 - \tau_r)^2} D_c \quad (15)$$

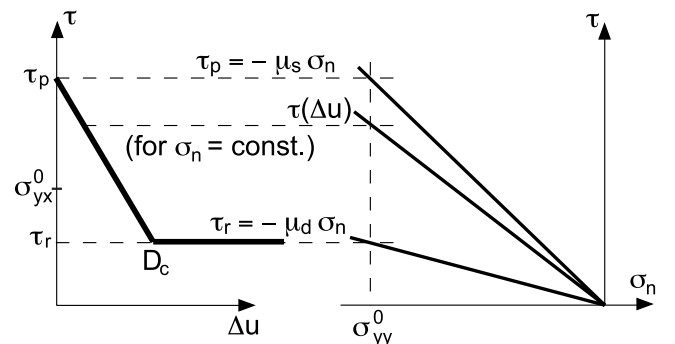


Figure 8. Slip-weakening Coulomb friction law. The peak and residual strength (τ_p , τ_r), and strength (τ) at any particular amount of slip (Δu), are proportional to normal compressive stress ($-\sigma_n$).

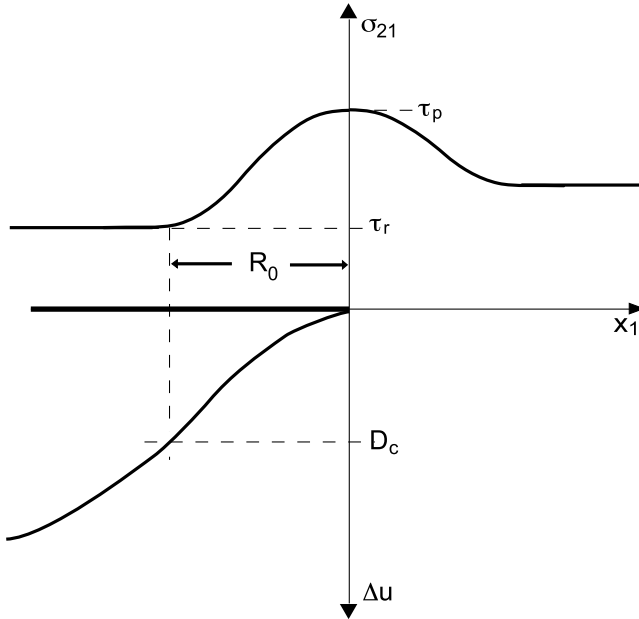


Figure 9. Fault and distribution of shear stress σ_{21} and slip displacement Δu .

Here, following the notation of *Kame et al.* [2003], L_c is the total length of the nucleating crack (not half length like by *Andrews* [1976]).

[53] The initial crack has to be long enough to permit the rupture to propagate along the fault but should be small compared to the fault length to not affect the dynamic results.

[54] In order to simply estimate R_0 , *Palmer and Rice* [1973] use another slip weakening law chosen to make τ vary linearly with x within the end zone. For the case when the end zone size is small in comparison to the other lengths such as the crack length and the minimum nucleation size, they determine

$$R_0 = \frac{3\pi}{8} \frac{\mu}{\tau_p - \tau_r} D_c \quad (16)$$

Rice [1980] pointed out that for the same slip weakening law, during dynamic propagation under locally steady state conditions on the scale of the end zone, the dynamic end zone size R is a function of the rupture velocity and diminishes with the velocity in particular way. That is,

$$R = \frac{R_0}{f(v_r)} \quad (17)$$

where $f = 1$ when $v_r = 0^+$ and $f(v_r)$ increase with v_r , without limit as $v_r \rightarrow c_R$, where $c_R = 0.9194 c_s$ (for $\lambda = \mu$) is the Rayleigh wave speed. In our model, we cannot calculate in closed form an exact value of the end zone length R . The results of equations (16) and (17) are quite realistic, according to mode II simulations by *Kame et al.* [2003] and our own results, and can often be used as estimation of the end zone size.

[55] Characteristics of the rupture velocity v_r attained during spontaneous dynamic propagation depend on S of

equation (2) [*Andrews*, 1976; *Das and Aki*, 1977]: $v_r < c_R$ always if S is above a threshold (1.7–1.8), but given enough propagation distance L when S is below that threshold, v_r will ultimately transition to the range $c_s < v_r < c_p$; L/L_c diverges at the threshold. In natural earthquake studied until now, the rupture velocity seems usually to be below the shear wave velocity. We have chosen $S = 1.3$ on the straight segment of the Kickapoo fault, which has the property that the maximal jumpable distance calculated in the static study is large enough but also that $v_r < c_R$ during the entire propagation along our representation of the Johnson Valley and Kickapoo faults.

4.3. Numerical Modeling of Dynamic Rupture: Boundary Integral Equation (BIE) Method

[56] The fault, represented by Γ in Figure 10, is approximated by a polygon consisting of elements of constant length Δs . The time is also discretized by a set of equally spaced time steps with an interval of Δt .

[57] The difficult step of the implementation is how to choose Δs according to our model. The size of the zone where the slip weakening Coulomb friction law is influential decreases from a static value R_0 , defined in section 4.2 to 0 as the rupture velocity increases. The smaller Δs is, the longer is the time when the law is properly represented. Once the size of the end zone R is too small, we are not suitably resolving the slip-weakening process and so cannot have confidence in the numerical result. Δs is chosen as a compromise between precision and time of calculation. In applications [e.g., *Koller et al.*, 1992; *Kame and Yamashita*, 1999] the ratio $c_p \Delta t / \Delta s$ has been chosen equal to 1/2. This value is smaller than $1/\sqrt{2}$, and therefore respects the stability conditions of corresponding two-dimensional finite difference methods, as explained by *Koller et al.* [1992].

[58] We use a discretized BIE to evaluate the changes in tangential and normal tractions, i.e., in σ_{21} and σ_{22} , respectively, on the faults due to dynamic slip. Those are changes relative to values in an initial static state at $t = 0$.

[59] Following earlier works by, e.g., *Andrews* [1985], *Das and Kostrov* [1987], *Koller et al.* [1992], *Cochard and Madariaga* [1994], *Tada and Yamashita* [1997], *Kame and Yamashita* [1999], and *Kame et al.* [2003], the displacement discontinuities along the fault are represented in the BIE using a piecewise constant interpolation. A constant slip velocity $V^{i,k}$, to be determined, is assumed within each spatial element (cell i of length Δs) and during each time step k , which runs from $(k-1)\Delta t$ to $k\Delta t$; here $k = 1, 2, \dots$. Since we start from a static state we set $V^{i,0} = 0$.

[60] The resulting expressions for $\sigma_{21}^{l,n}$ and $\sigma_{22}^{l,n}$, at the center of cell l at the end of time step n , are

$$\sigma_{21}^{l,n} = -\frac{\mu}{2c_s} V^{l,n} + \sum_{k=0}^{n-1} \sum_i V^{i,k} K_t^{l,i,n-k} + \sigma_{21}^{l,0}, \quad (18)$$

$$\sigma_{22}^{l,n} = \sum_{k=0}^{n-1} \sum_i V^{i,k} K_n^{l,i,n-k} + \sigma_{22}^{l,0} \quad (19)$$

for $n = 1, 2, \dots$. Here $K^{l,i,n-k}$ represents the stress at the center of cell l , at the end of time step n due to a unit slip velocity within cell i during time step k . These kernels can be

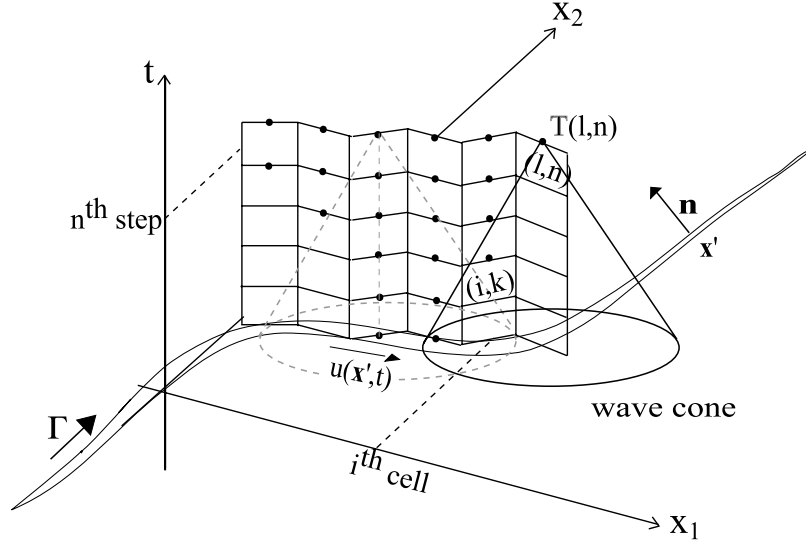


Figure 10. Nomenclature used in the crack analysis and schematic diagram of the discretized BIE method. The points represent the cells with non zero slip velocity.

calculated analytically in 2-D by appropriate integrations of the stress field in response to impulsive point double couples. Also, $K_t^{l,i,0} = -\mu/(2c_s)$ when $i = l$ and is 0 otherwise, given that our Δt is less than a p wave travel time over a cell; $\mu/(2c_s)$ is the radiation damping factor or fault impedance [Cochard and Madariaga, 1994; Geubelle and Rice, 1995] and represents the instantaneous contribution of the current slip velocity to the shear stress at the same position. $K_n^{l,i,0} = 0$ is zero because we consider no opening along the fault. Also, $\sigma_{21}^{l,0}$ and $\sigma_{22}^{l,0}$ are the tractions in the static initial state at $t = 0$. Because of the properties of wave propagation, the convolution sums have to be done only for those cells i and prior time steps k that fall inside the p wave cone of l, n , as illustrated in Figure 10.

4.4. Nucleation of the Rupture

[61] In order to nucleate dynamic rupture, we first assume [Kame *et al.*, 2003] a nucleation zone in a static equilibrium state (corresponding to the state at $t = 0$ discussed in section 4.3) on the Johnson Valley-Kickapoo fault whose slip respects the slip-weakening boundary condition. We allow slip in a region of length L_{nuc} slightly larger than the minimum nucleation size L_c given by equation (15) but prevent slip outside this region until $t > 0$, so that a dynamic rupture begins with nonnegligible slip rate at the crack tip at time step $n = 1$. The static equilibrium is found when the slip and the stress field due to the initial stress and the slip in the nucleation region satisfies the slip-weakening law.

[62] If the nucleation zone consists of N cells, then their N unknown preslips D^l (the notation D is synonymous with Δu) alter the tectonic prestress $(\sigma_{21}^0)_{\text{pre}}^l$ at the center of cell l to a new static stress

$$\sigma_{21}^l = \sum_i D^i K_{t,\text{static}}^{l,i} + (\sigma_{21}^0)_{\text{pre}}^l \quad (20)$$

That σ_{21}^l will be identified as the term $\sigma_{21}^{l,0}$ in dynamic representation equation (18). Here $K_{t,\text{static}}^{l,i}$ is the corresponding static stress kernel. Because we nucleate here along a straight segment of the fault, that kernel depends there only

on $l - i$. Also, sliding gives no change in the normal stress on that same planar segment from its value $(\sigma_{22}^0)_{\text{pre}}$ due to the prestress field.

[63] We must choose the D^l for the N cells of the nucleation zone so that stresses at each cell are consistent with the slip-weakening strength of equations (13) and (14) and Figure 8. That is, if the law is represented as $\tau = -\sigma_n F(\Delta u)$, then we require that the σ_{21}^l for the N cells also satisfy

$$\sigma_{21}^l = -(\sigma_{22}^0)_{\text{pre}}^l F(D^l) \quad (21)$$

The solution of equations (21) and (20) is numerically determined using the Newton-Raphson method. The resulting slips D^l are identified as $D^{l,0}$, i.e., at time 0, for the dynamic analysis.

[64] The distribution of slip along this initial nucleation region causes an initial stress concentration which is slightly larger than the peak strength at the both tips of the zone and so enables propagation of the rupture at the first dynamic time steps.

4.5. Rupture Dynamics Procedures

[65] At time 0^+ , we begin the dynamic analysis. For $n = 1, 2, \dots$, stresses at the end of the n th time step are determined in terms of slip rates $V^{i,k}$ by

$$\sigma_{21}^{l,n} = -\frac{\mu}{2c_s} V^{l,n} + (\sigma_{21}^{l,n})_{\text{past}} \quad (22)$$

$$(\sigma_{21}^{l,n})_{\text{past}} = \sum_{k=0}^{n-1} \sum_i V^{i,k} K_t^{l,i,n-k} + \sum_i D^{i,0} K_{t,\text{static}}^{l,i} + (\sigma_{21}^0)_{\text{pre}}^l \quad (23)$$

$$\sigma_{22}^{l,n} = \sum_{k=0}^{n-1} \sum_i V^{i,k} K_n^{l,i,n-k} + \sum_i D^{i,0} K_{n,\text{static}}^{l,i} + (\sigma_{22}^0)_{\text{pre}}^l \quad (24)$$

and, of course, slips are updated to the end of the step by $D^{l,n} = D^{l,n-1} + \Delta t V^{l,n}$. Here $(\sigma_{21}^{l,n})_{\text{past}}$ is the stress at time $n\Delta t$

due to the history of slip everywhere up to time $(n-1)\Delta t$; it is equal to $\sigma_{21}^{l,n}$ for cells which do not slip in that n th time step.

[66] To solve for the slip rate in each time step, we assure that the stresses and slip at the end of that step precisely satisfy the slip-weakening constitutive law. Thus, as in equations (13) and (21), let $\tau = -\sigma_n F(\Delta u)$ represent the strength. Then if

$$\left(\sigma_{21}^{l,n}\right)_{\text{past}} < -\sigma_{22}^{l,n} F(D^{l,n-1}) \quad (25)$$

we must set $V^{l,n} = 0$, which is consistent with $D^{l,n} = D^{l,n-1}$ and $\sigma_{21}^{l,n} = (\sigma_{21}^{l,n})_{\text{past}}$. For the cells at each rupture tip, that test becomes $(\sigma_{21}^{l,n})_{\text{past}} < -\sigma_{22}^{l,n} F(0) = -\mu_s \sigma_{22}^{l,n}$ and, if met, it means that the rupture front does not advance in that time step.

[67] On the other hand, for all cells satisfying

$$\left(\sigma_{21}^{l,n}\right)_{\text{past}} \geq -\sigma_{22}^{l,n} F(D^{l,n-1}) \quad (26)$$

we must choose $V^{l,n}$ to satisfy

$$\left(\sigma_{21}^{l,n}\right)_{\text{past}} - \frac{\mu}{2c_s} V^{l,n} = -\sigma_{22}^{l,n} F(D^{l,n-1} + \Delta t V^{l,n}) \quad (27)$$

Kame et al. [2003] stated conditions on Δt to ensure that there exists a unique solution of equation (27) satisfying $V^{l,n} \geq 0$. For the linear slip-weakening law adopted here, that reduces to

$$\frac{\mu}{2c_s} > -\sigma_{22}^{l,n} (\mu_s - \mu_d) \frac{\Delta t}{D_c} \quad (28)$$

(It assures, e.g., that if there is equality in (26), then the obvious solution $V^{l,n} = 0$ is the only possible one.) For the linear law the solution is readily written out explicitly, with different forms depending on whether $D^{l,n-1} < D_c$ or $D^{l,n-1} \geq D_c$. In the latter case the result is just $V^{l,n} = (2c_s/\mu) [(\sigma_{21}^{l,n})_{\text{past}} + \mu_d \sigma_{22}^{l,n}]$. Thus we determine the slip velocity on each fracturing element.

[68] If we use the definition of the different parameters given earlier, the above inequality (equation (28)) assuring a unique nonnegative slip velocity becomes [*Kame et al.*, 2003]:

$$\Delta s/R_0 < 8/(\sqrt{3}\pi) \quad (29)$$

i.e., $\Delta s/R_0 < 1.47$. Here, however, it is important to understand that the R_0 , which scales inversely with $\tau_p - \tau_r$ [= $(\mu_s - \mu_d) (-\sigma_n)$] as in equation (16), must be evaluated with σ_n equated to the momentary normal stress $\sigma_{22}^{l,n}$. That is not constant in time for propagation along branched or curved faults, and the criterion, which must be satisfied all along the rupturing zone(s) considered, can only be tested for certain during the solution itself (which may then have to be redone with a more refined Δs , and hence Δt). This is important in propagation along faults which curve toward the compressional side of the advancing rupture, because that locally increases the fault-normal compression and can

invalidate the choice of a Δs that seemed acceptable in terms of the prestress field.

4.5.1. Regularization: Smoothing the Slip Rate Distribution

[69] Following *Yamashita and Fukuyama* [1996], we introduce what they call “artificial attenuation” to eliminate short-wavelength oscillations which appear in slip velocity, due to the abrupt progress of the fracture front along the discretized fault trace. The oscillations only gradually become evident for large numbers time steps, but then they grow rapidly, and invalidate the results [*Yamashita and Fukuyama*, 1996; *Kame and Yamashita*, 1999; *Kame et al.*, 2003]. We likewise try to eliminate the oscillations by their regularization procedure. Thus, after calculating the slip velocity V over the ruptured region, at each time step, n , we transform it to a smoothed one by

$$V_{\text{sm}}^{i,n} = V^{i,n} + \alpha (V_{\text{sm}}^{I-1,n} + V_{\text{sm}}^{i+1,n} - 2V_{\text{sm}}^{i,n}) \quad (30)$$

The unknown $V_{\text{sm}}^{i,n}$ is then solved for numerically, along the currently ruptured zone where $V^{i,n} \geq 0$ (but with $V_{\text{sm}}^{i,n}$ set to 0 for all cells where $V^{i,n} = 0$), using a matrix inversion. The $V_{\text{sm}}^{i,n}$ are then used to redefine $V^{i,n}$ for updating the slip and doing future convolution sums.

[70] The choice of the smoothing factor α is delicate: stronger smoothing suppresses not only the oscillations but the amount of slip. A compromise has to be made between stability and plausibility of the solution. Comparing their numerical results using this procedure with an analytical solution, *Yamashita and Fukuyama* [1996] have shown that the value $\alpha = 1/2$ gives stable and reasonably accurate results. This value is chosen for our simulations.

4.5.2. Procedures for Rupture Transfer to the Second Fault

[71] We will apply our procedures to study rupture along the Johnson Valley-Kickapoo fault and then address whether and how rupture could jump to the second fault, the Homestead Valley fault. As shown by *Harris and Day* [1993], three scenarios are possible, depending on the geometrical characteristics of the faults: (1) The rupture dies at the end of the first fault segment. (2) The rupture triggers on the second fault segment but cannot absorb enough energy to propagate. (3) The rupture triggers the second fault segment and then continues propagating.

[72] With the slip rate history of the first fault given from a prior calculation, we study the possibility for the rupture to jump, considering time steps when the rupture has not yet completed on the first fault. We calculate the tangential and normal tractions all along the second fault for each time step, understanding that slip, if not a propagating rupture, can nucleate when in one cell the tangential traction is higher than the local peak strength. If this happens, in section 4.5 we apply the algorithm explained above for the calculation of slip velocity in the ruptured region and the propagation of the rupture. To reduce computation time we suppose that the rupture on the second fault has no influence on the first; that means that we do not calculate the change of the stress on the first fault due to the rupture on the second one. This is sensible because slip on the first fault has stopped or nearly stopped by the time waves from any

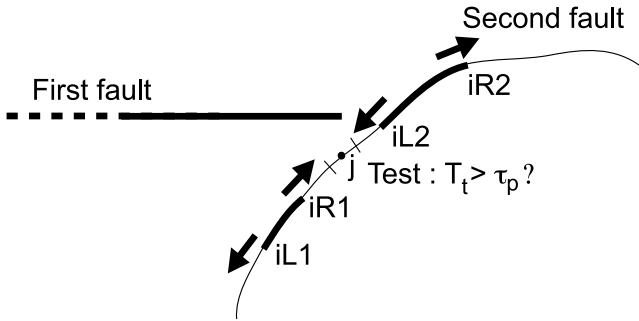


Figure 11. Multiple nucleations. The first fault has ruptured. The iL and iR represent the left and the right tips, respectively, of each ruptured region.

small further slip on the first fault made their way back to the second, the rupture front would have moved much further along the second fault.

[73] Depending on the geometry of the second fault, multiple nucleation sites may exist, as showed in the static study. A rupture can nucleate in different time steps and at different isolated locations. So, if a rupture has already nucleated, we continue to test along the region which has not ruptured if a nucleation is possible (Figure 11). If two nucleations are possible for example, we just must take care to join the tips ($iL(i)$ and $iR(j)$ represented in Figure 11) of the two ruptured regions when it is possible. For the propagation of the rupture and the calculation of slip velocities for each region, the same algorithm as above is used.

5. Rupture Along the Johnson Valley and Kickapoo Faults

[74] The nucleation is simulated near the center of the Johnson Valley segment of the fault around cell -150 (represented by a circle in Figure 7). According to the

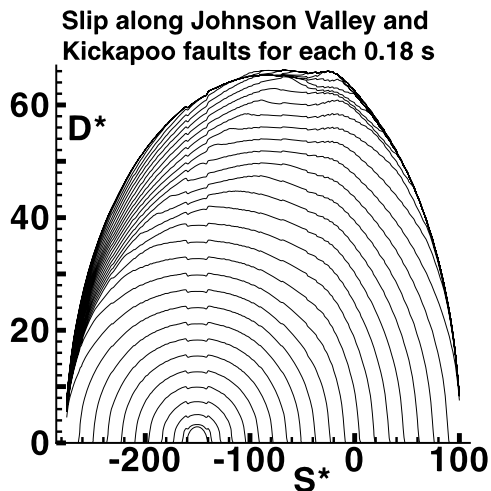


Figure 12. Along Johnson Valley and Kickapoo faults, slip Δu (as $D^* = 3\mu\Delta u/(-\sigma_{yy}^0 R_0^0)$) versus $s^* = 3s/R_0^0$ where s is the curvilinear coordinate) for each 0.18 s (that is $9R_0^0/c_p$).

prestress σ_{ij}^0 and the 26° orientation of the fault around this location, equation (15) determines the minimum nucleation size as $L_c = 5\Delta s$. That is about $2R_0$, which does not fully respect the assumption needed to validate equation (15) (R_0 should be much smaller than L_c). To enable the initiation of the rupture, the length of the initial crack is taken as $L_{\text{nucl}} = 20\Delta s$.

[75] The rupture propagates bilaterally along the Johnson Valley segment and continues along the curved part and along the Kickapoo fault, as shown in Figures 12 and 13, which represent the slip Δu (as $D^* = 3\mu\Delta u/(-\sigma_{yy}^0 R_0^0)$) for each 0.18 s (that is $9R_0^0/c_p$) and the slip velocity V , respectively (as $V^* = \mu V/(-\sigma_{yy}^0 c_p)$) for several time steps ($N = 6c_p t/R_0^0$), all along the fault (as $s^* = 3s/R_0^0$ where s is the curvilinear coordinate). Here the scale length R_0^0 refers to the static end zone size R_0 as calculated from the normal prestress on the straight part of the Landers fault; R_0 depends on the orientation considered. Note that the slight

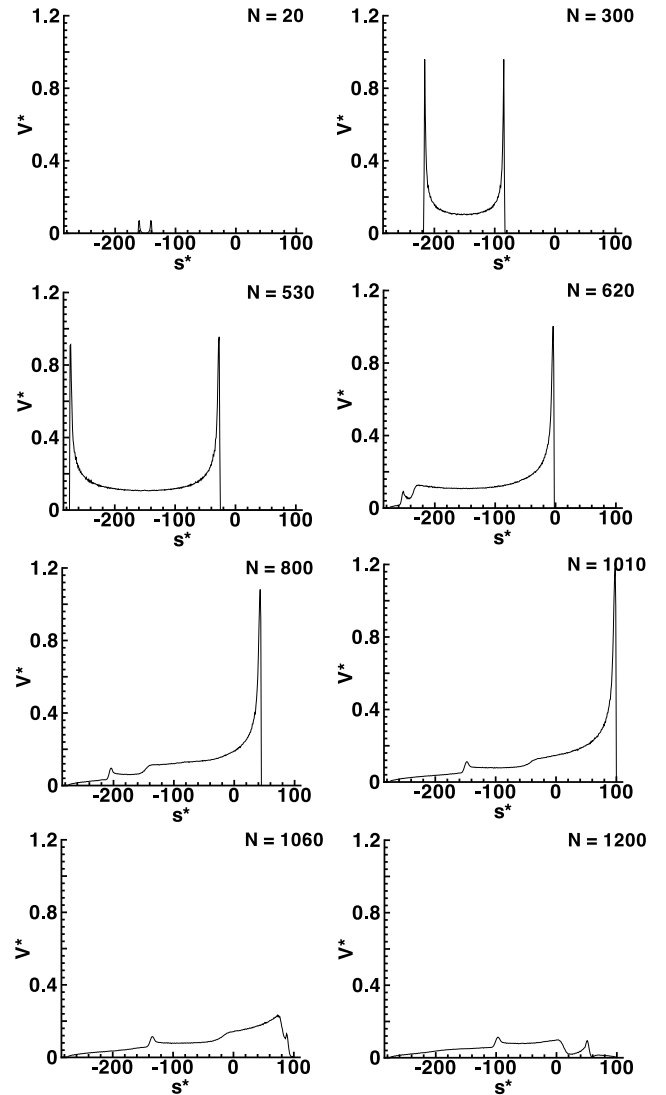


Figure 13. Along Johnson Valley and Kickapoo faults. Slip velocity V (as $V^* = \mu V/(-\sigma_{yy}^0 c_p)$) versus $s^* = 3s/R_0^0$ where s is the curvilinear coordinate) for several time steps $N = 6c_p t/R_0^0$.

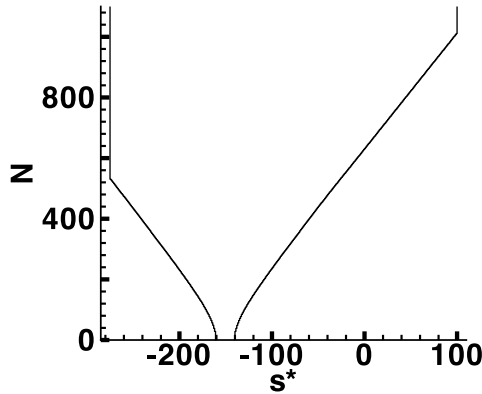


Figure 14. Position of the left and right ends of the ruptured zone along Johnson Valley and Kickapoo (as $s^* = 3s/R_0^*$, where s is the curvilinear coordinate, the origin is the beginning of the part of the fault parallel to the x axis) for each time step (as $N = 6c_p t/R_0^*$). The two lines at each edge indicate the length of the ruptured zone. The length of the right part of the fault is about 4 km ($s^* = 100$); the length of the left part is about 11 km ($s^* = -275$).

decrease in slip at the nucleation location is an artifact of the nucleation process. Actually, the rupture reaches the SSE end of the region of Johnson Valley fault modeled at $N = 531$ (1.77 s). Going NNW, it reaches the curved part (at cell -50) at time step $N = 437$ (1.47 s), the straight part of Kickapoo fault at $N = 629$ (2.1 s) and its end at $N = 1011$ (3.37 s).

[76] The slip velocity increases slightly along the curved part and it is higher along the Kickapoo than along the Johnson Valley fault. This is partly because of the decrease of the normal stress along the fault and because the ruptured zone is getting longer. We notice too that as we wanted at the beginning, reaching the SSE end of Johnson Valley seems to have no influence on the propagation of the rupture at the other end. After slipping, the end of the Kickapoo fault seems to lock very rapidly and stop slipping, which is represented between the time $N = 1060$ and $N = 1200$ but continues after.

[77] According to the representation of slip (Figure 12) the maximum of slip is ~ 4.4 m. The average along Johnson Valley is ~ 3.3 m, whereas *Hardebeck and Hauksson* [2001] reported it as 2.0 ± 0.5 m. The difference is likely because of the assumptions of the slip weakening model and perhaps because of the simplicity of the prestress field and the 2-D approximation itself. The average predicted along Kickapoo is about 3.6 m.

[78] As shown in Figures 12 and 13, the rupture is not inhibited by the curvature of the fault toward its extensional side (an inhibiting effect of curving away from the extensional side will be seen later for the SSE Homestead Valley fault). This is consistent with the results of *Kame et al.* [2003] which suggest that for this orientation of the compressive principal stress, rupture along the branch (Kickapoo fault) is favored.

[79] Figure 14 represents the propagation of each tip of the ruptured zone. The velocity of the right tip does not change when it reaches the curved part ($s^* = -50$) or the straight part parallel to the x axis ($s^* = 0$). The rupture

velocity v_r , represented in Figure 15 (as v_r/c_s) increases and keeps a roughly constant value along the curved and the straight parts. That is around $0.9c_s$, i.e., very close to c_R . The v_r reported by our procedures is in the form $3\Delta s/n\Delta t$ where n is the number of time steps for the rupture to advance by 3 cell sizes; hence v_r is always quantized, as in Figure 14.

6. Does the Rupture Jump From the Kickapoo Fault to the Homestead Valley Fault?

[80] Using the slip history rate of the Johnson Valley-Kickapoo fault, we want to know now if a rupture, or more than one, can nucleate along the Homestead Valley fault, and if it does, if it propagates bilaterally or not and finally what is the influence of the geometry on the propagation.

6.1. Stress Distribution Near the Homestead Valley Fault

[81] We first ignore rupture on that latter fault, and simply evaluate the stresses radiated from the first one, and if and where they are large enough to initiate slip weakening elsewhere. For that we have considered a region (contoured in Figure 16) with the same local orientation as the Homestead Valley fault, with the same length and a thickness of 320 m (8 cells). The Homestead Valley fault is in the center of the region. For purposes of defining stress components on the 1, 2 system, the 2 direction at any point in the region is the local perpendicular direction to the Homestead Valley fault. The quantity $\sigma_{21}/(-\mu_s \sigma_{22})$ is contoured for several time steps in Figure 16.

[82] First, we notice something which does not happen in the stress distribution around the straight fault for parallel elements described in the static study: this is the region which moves from the time step $N = 800$ to $N = 1200$ and which represents a negative ratio $\sigma_{21}/(-\mu_s \sigma_{22})$. (The static study in the first part suggests that a tensile domain ($\sigma_{22} > 0$) will not exist in the region now studied.) Indeed, the calculations show that for these regions the shear stress is negative which would imply a left-lateral slip if the ratio ever becomes

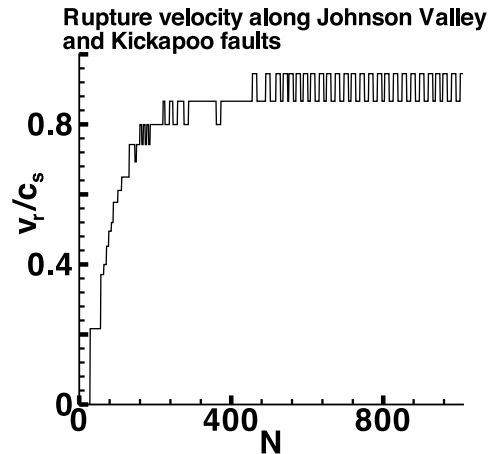


Figure 15. Rupture velocity v_r (as v_r/c_s) between the initiation of the rupture and the moment when it reaches the end of Kickapoo fault (in terms of time step $N = 6c_p t/R_0^*$) along first the Johnson Valley fault and afterward Kickapoo fault.

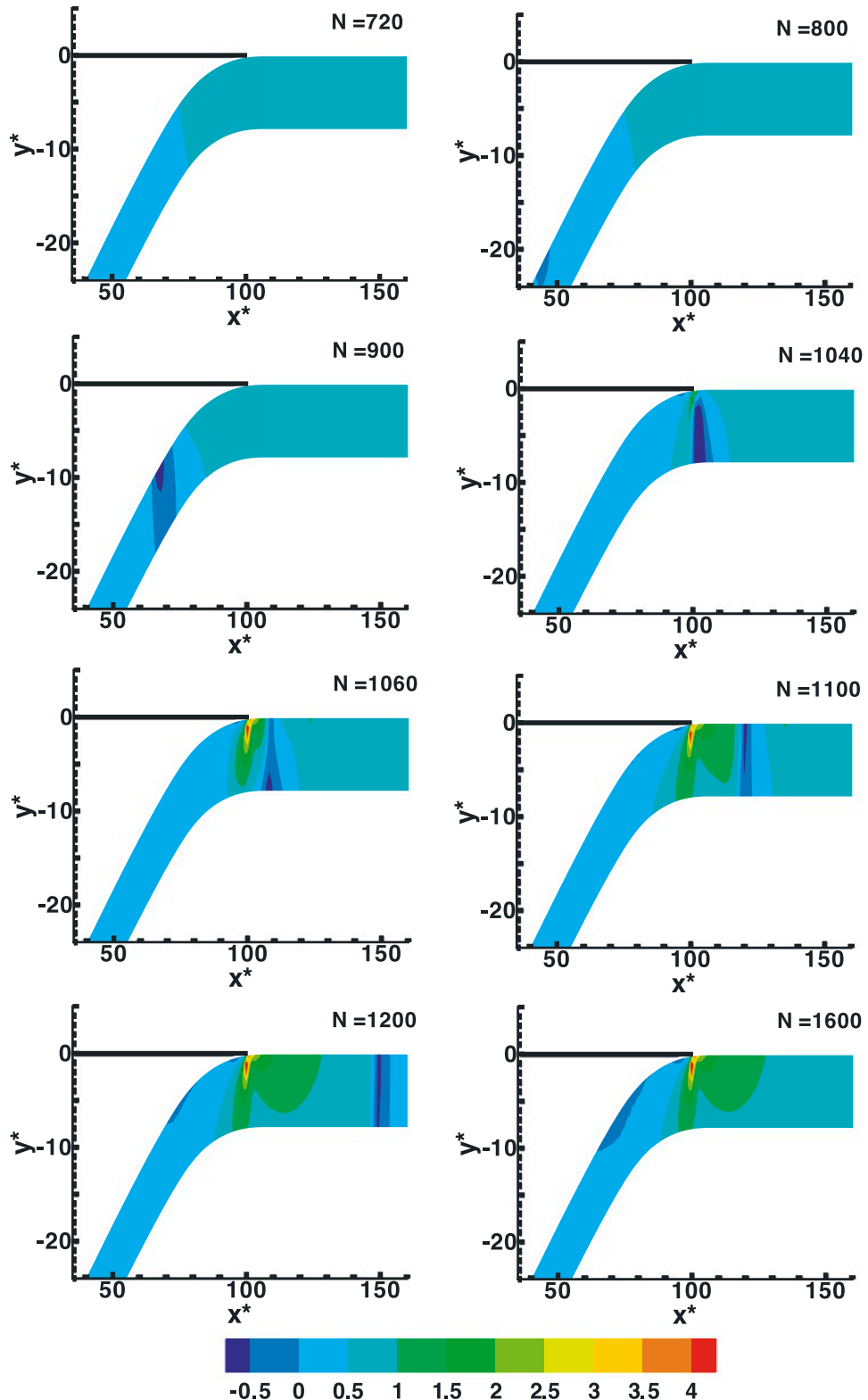


Figure 16. Stress distribution around Homestead Valley fault for elements locally parallel to it. The contoured quantity is $\sigma_{21}/(-\mu_s \sigma_{22})$, where (x_1, x_2) are the tangential and the normal directions relative to the Homestead Valley fault (see text). Here $x^* = 3x/R_0^o$ and $y^* = 3y/R_0^o$. Representation for several time steps is $N = 2c_p t/R_0^o$.

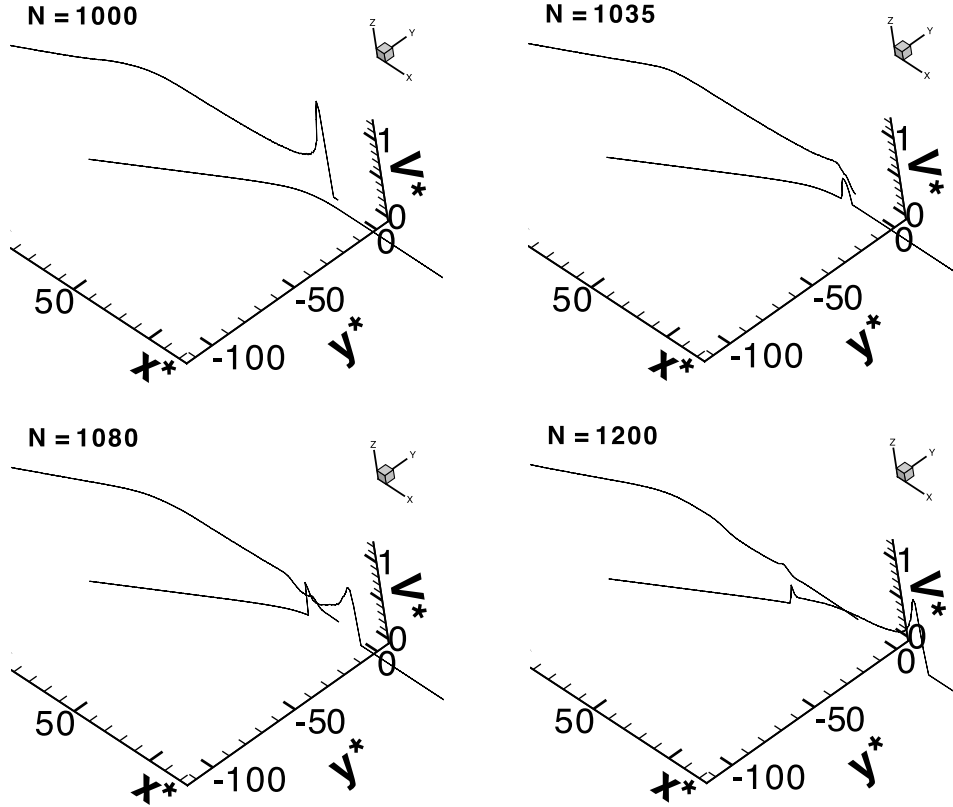


Figure 17. Slip velocity V (as $V^* = \mu V/(-\sigma_{yy}^0 c_p)$) versus $x^* = 3x/R_0^0$ and $y^* = 3y/R_0^0$ for several time steps $N = 4c_p t/R_0^0$, along the faults, around the step over.

more negative than -1 . Only right-lateral slip was allowed in our calculation.

[83] The critical value of 1 for the ratio $\sigma_{21}/(-\mu_s \sigma_{22})$ (which means that a rupture is possible) is first reached in the curved part around the time step $N = 1040$. The region where the rupture is possible expands especially in the straight part and keeps a constant shape after the time step $N = 1300$ which is shown in the last picture. Note that there is reasonable correspondence, at the longer times shown here, of the region $\sigma_{21}/(-\mu_s \sigma_{22}) > 1$ and the static prediction of that region in Figure 6.

6.2. Stopping as an Aid to Jumping

[84] We can see in Figure 16 that a rapidly propagating rupture is much more effective at generating high stresses on parallel, or roughly parallel, nearby faults once its propagation has been abruptly stopped by a barrier than it was just before that blockage. For example, the rupture reaches the barrier formed by the northern termination of Kickapoo, moving at high speed, at time step $N \approx 1000$. As Figure 16 shows, it is only some time later, as something resembling the static field of Figure 6 starts to develop, that a large region near the fault experiences failure level stressing near the rupture tip.

[85] Thus it is much more likely for rupture to jump from a first to a roughly parallel second fault if its propagation has been abruptly stopped on the first. Jumps not associated with sudden slowing of propagation on the first fault are expected to be rare in nature. These observations are in accord with a basic result of dynamic crack theory for the

singular model [Fossum and Freund, 1975], namely, that the stress intensity factor at a rapidly propagating crack tip increases significantly when that propagation is suddenly stopped. A case of rupture jumping when rupture velocity slows (rather than stops) is examined in Oglesby et al. [2003a], and other cases of rupture jumping between faults are examined by Harris et al. [1991] and Harris and Day [1993, 1999] as mentioned earlier, as well as in Yamashita and Umeda [1994], Kase and Kuge [1998, 2001], Harris et al. [2002] and Oglesby et al. [2003b].

[86] We can conclude from this analysis that a rupture is likely to nucleate along the Homestead Valley fault and perhaps in several location. Further, stresses large enough to initiate right-lateral slip weakening ultimately extend over the entire region between the Kickapoo and Homestead Valley faults.

6.3. Jump of the Rupture and Bilateral Propagation

[87] The last calculations lead to the possibility of multiple nucleation along the second fault. However, as a matter of fact, a detailed calculation of the rupture shows that it nucleates at a single location: along the curved part at cell -8 ($x^* = 99$ and $y^* = -4.18$), which is just below the termination of Kickapoo (in terms of x^* , y^* , the end of the Kickapoo fault is at $x^* = 100$ and $y^* = 0$) and which has an orientation of $\omega = 2.8^\circ$. The initiation of slip occurs at $N = 1022$ (3.4s) and rupture starts propagating bilaterally, almost instantaneously, at $N = 1028$ (3.43 s). Figure 17 represents the slip velocity V (as $V^* = \mu V/(-\sigma_{yy}^0 c_p)$) along the Kickapoo and Homestead Valley faults represented in the x - y plane

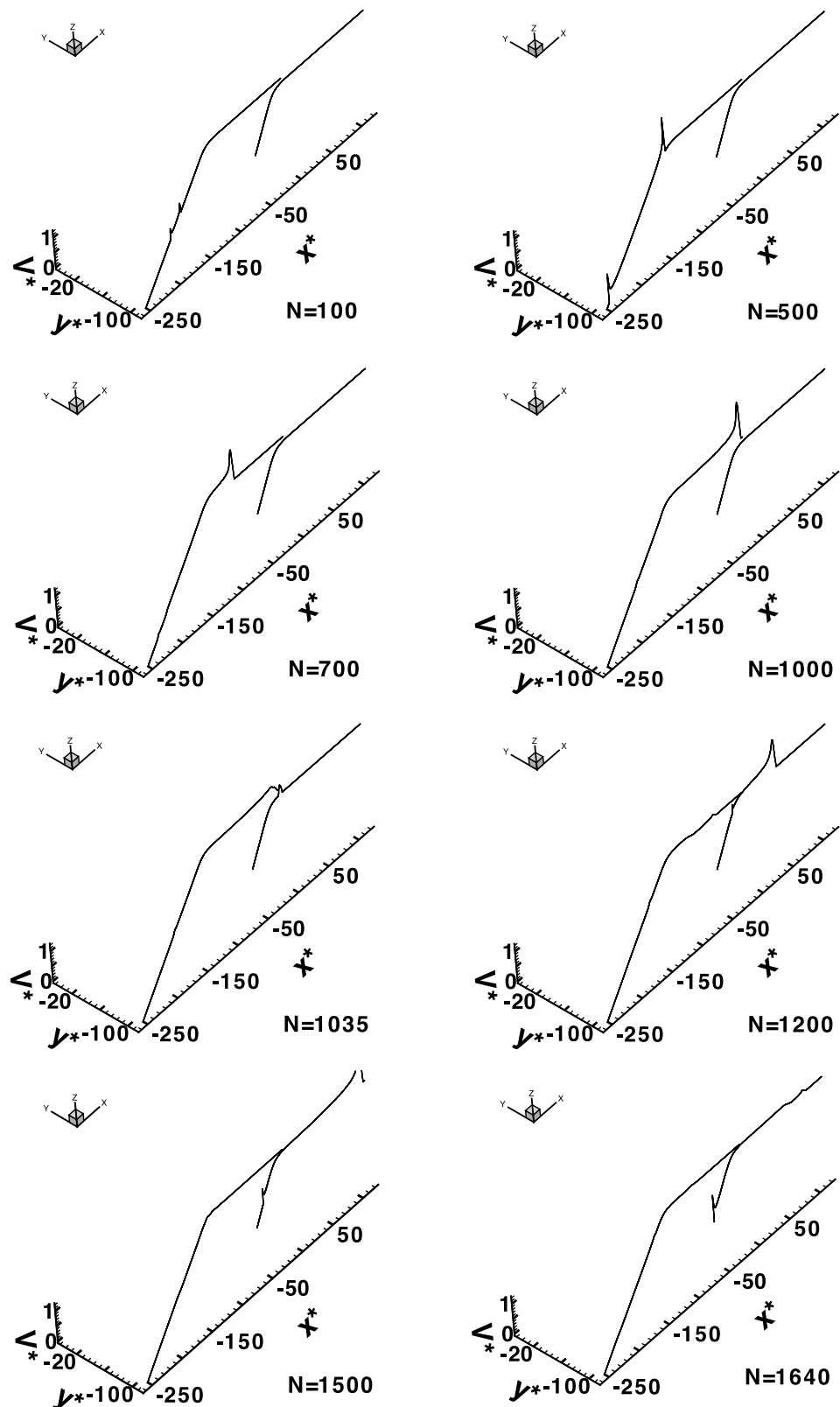


Figure 18. Slip velocity V (as $V^* = \mu V / (-\sigma_{yy}^0 c_p)$) versus $x^* = 3x/R_0^0$ and $y^* = 3y/R_0^0$ for several time steps $N = 4c_p t/R_0^0$, along the faults.

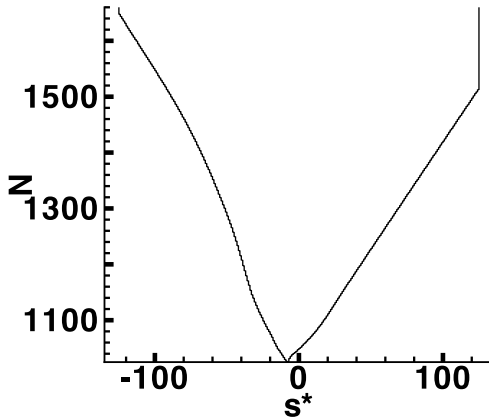


Figure 19. Position of the left and right ends of the ruptured zone (as $s^* = 3s/R_0^o$, where s is the curvilinear coordinate, the origin is the center of Homestead Valley fault) for each time step (as $N = 6c_p t/R_0^o$). The two lines at each edge indicate the length of the ruptured zone. The half length of the fault is fixed to about 5 km ($s^* = 125$).

around the step over before and after the jump. Figure 18 represents the slip velocity and so the rupture propagation at larger scale, along Johnson Valley and Kickapoo, and finally Homestead Valley, showing all the modeled region.

[88] The rupture propagates bilaterally on the Homestead Valley fault: forward along the straight part parallel to the Kickapoo fault and backward along the curved part and then the straight part at orientation $\omega = 30^\circ$. The rupture velocity slows down noticeably along the curved part of the Homestead Valley fault, as shown in Figure 19. The northern end of the ruptured zone moves forward more quickly than the SSE end, which has to contend with the curvature, which in this case is away from the extensional side. The effect is to increase normal stress along that curved part. *Bouchon and Streiff* [1997] have investigated rupture of a curved fault similar to the Homestead Valley fault, and also found a reduction in rupture velocity and slip. In more severe cases it is clear that such adverse curvature could arrest rupture propagation, although that does not happen in this case.

[89] Forward, the rupture reaches the end at $N = 1513$ (5.04 s) of the northern portion of the Homestead Valley fault modeled. The actual rupture did not end there (instead continuing well to the NNW), but its stoppage in the simulation is too late for waves from that to compromise the modeling of the propagation to the SSE. Backward, it finishes crossing the curved part at $N = 1287$ (4.29 s). Its velocity increases again (as the discontinuity of the line at the cell -50 suggests) and then remains roughly constant along the oblique straight part. It reaches the end of the SSE zone at $N = 1648$ (5.49 s), leaving in its wake the backward branch which motivated our study.

[90] Figure 20 compares the slip velocity along the different part of the fault. It is higher along the straight part than along the curved part where it decreases dramatically. However, when the rupture reaches the oblique straight part, the slip velocity increases again but remains lower than the section with an orientation parallel to the x axis. Besides, as remarked, the end of the rupture forward has no influence for the rupture backward.

[91] Finally, Figure 21 represents the slip Δu (as $D^* = 3\mu\Delta u/(-\sigma_{yy}^0 R_0^o)$) all along the fault (in terms of cells $s^* = 3s/R_0^o$). It is not the location of nucleation which corresponds to the maximum slip (~ 4 m) but rather the region around cell -10 . That corresponds to the beginning of the straight north directed segment which is close to the nucleation site and on which high shear stress is applied, as the stress distribution around the fault (Figure 16) suggests. The average of slip is ~ 2.4 m. We thus observe the high drop of slip along the adversely curved part. The rupture would stop if the fault did not stop curving, both because of the induced compressional normal stress discussed and because of increasingly unfavorable orientation relative to the prestress field.

7. Discussion and Conclusions

[92] Our work has addressed the relation between fault branches left after a large, complex earthquake and rupture directivity in the event. For that we investigated a new dynamic mechanism which leaves behind a feature that looks like a backward fault branch, that is, a branch directed opposite to the primary direction of rupture propagation. The mechanism consists of the stopping of the rupture on one fault strand and jumping to a neighboring strand, by stress radiation to it and nucleation of rupture on it which propagates bilaterally. Rare as such a feature might be, it could mislead observers attempting to understand the directivity of a past complex earthquake [Nakata *et al.*, 1998]. We conclude that it is difficult to judge the directivity of the main event from the pattern of branches it left and that additional understanding of the structure near the fault junction is needed to reach definitive conclusions.

[93] We analyze a field example of a backward fault branch formed during the Landers 1992 earthquake, when rupture propagating along the Kickapoo fault stopped at the end of that strand and then jumped to the Homestead Valley fault, where it developed bilaterally. The southern end of the Homestead Valley rupture formed a backward branch, while the main rupture continued NNW. We have no observational proof, other than the clear patterns of damage to a particular side of the Southern Homestead Valley fault (see Figure 2 and Poliakov *et al.* [2002]), that this is what really happened; existing analysis of coseismic observations have not clarified that picture. It is even possible to assume that the southern end of the Homestead Valley fault broke in an early aftershock. However, we have developed relevant theory for rupture transfer, and have simulated such a mechanism numerically, with a simplified geometry of the region under discussion.

[94] We conclude that what we describe is definitely possible mechanically, that it very plausibly was the rupture mechanism in the Kickapoo to Homestead Valley transition, and that it could act more generally in other large earthquakes which rupture through complex fault systems. This means that caution is needed when relating fault branches of past earthquakes with their directivity. Simple forward branching, even if probably most common, might not be the only branching mechanism.

[95] Our work has broadened the mechanical analysis of fault jumping, the basis of which is due to *Harris *et al.** [1991], *Harris and Day* [1993] and *Harris and Day* [1999] who numerically analyzed ruptures jumping between paral-

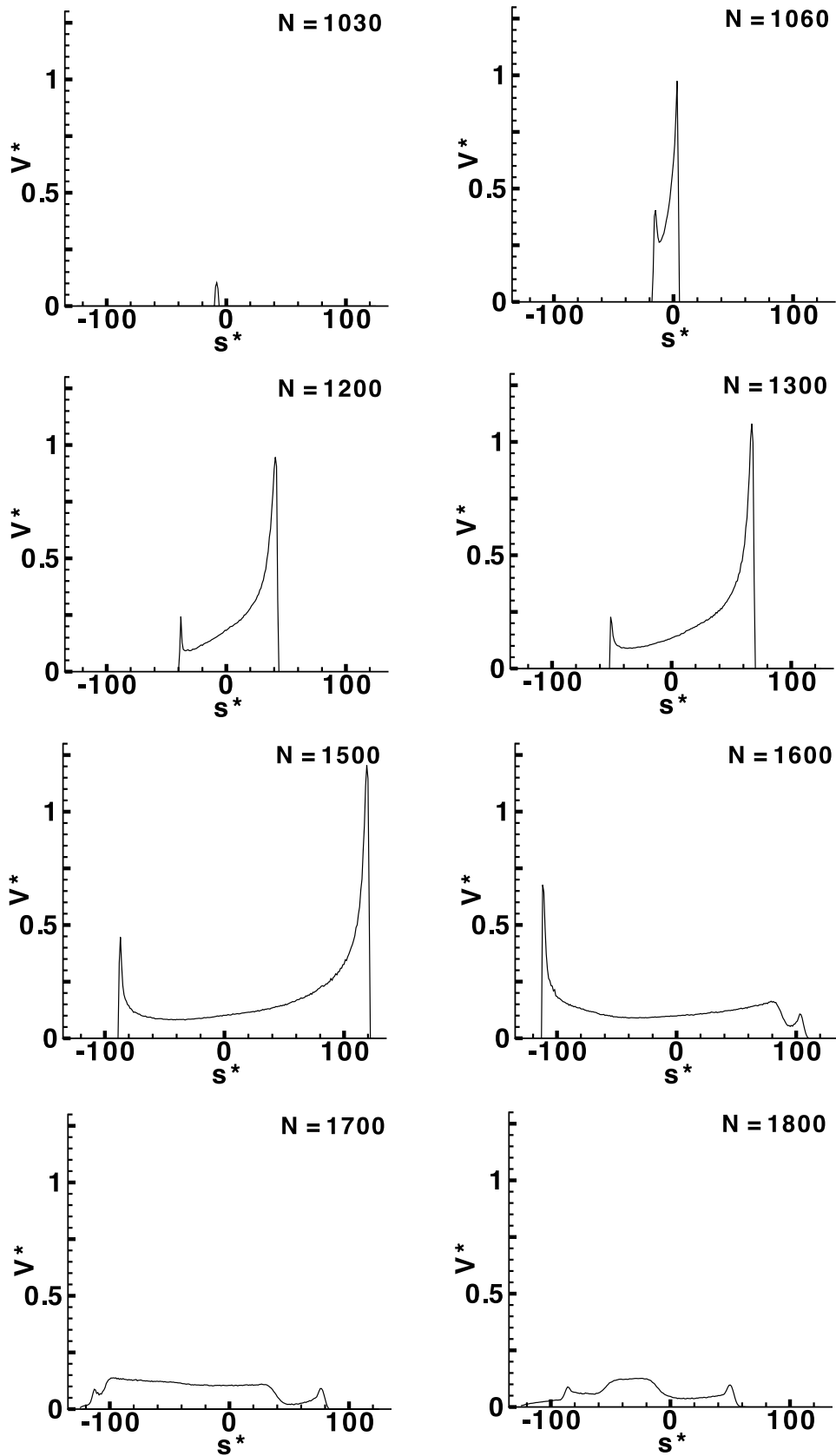


Figure 20. Along the Homestead Valley fault, slip velocity V (as $V^* = \mu V / (-\sigma_{yy}^0 c_p)$) versus $s^* = 3s/R_0^o$, where s is the curvilinear coordinate) for several time steps $N = 6c_p t/R_0^o$.

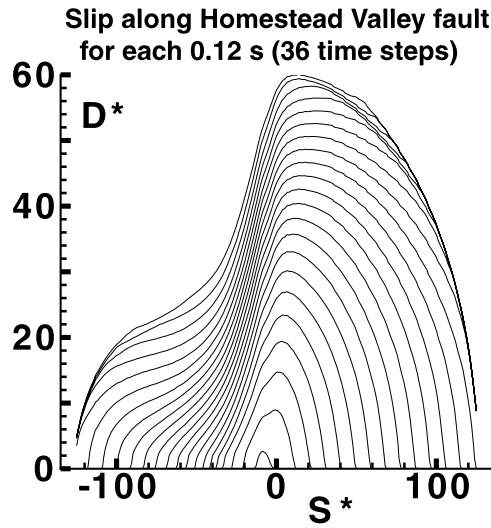


Figure 21. Along the Homestead Valley fault, slip Δu (as $D^* = 3\mu\Delta u/(-\sigma_{yy}^0 R_0^0)$) versus $s^* = 3s/R_0^0$, where s is the curvilinear coordinate) for each 0.18 s (that is $9R_0^0/c_p$).

lel faults. Here we analyzed ruptures jumping onto possibly nonparallel faults, and subsequent propagation along gradually curving faults, using the elastodynamic boundary equation (BIE) method with a Coulomb type of slip weakening. A fully systematic analysis of such jumps has to be left for future work. However, we can offer some insights into the mechanics of such jumps.

[96] First, it seems important that the rupture on the main fault stops or at least slows down if successful transfer of rupture to the neighboring, nonparallel fault is to be accomplished. This is because the stress concentration carried by the rupturing front diminishes with rupture velocity [Fossum and Freund, 1975] and is largest when propagation stops.

[97] We showed that stresses radiated to the curved Homestead Valley fault, while the rupture tip was still propagating along the Johnson Valley-Kickapoo fault system, would be unlikely to nucleate rupture on the Homestead Valley fault. Rather, the jump was made possible by the much higher stresses radiated when the rupture stopped at the northern termination of the Kickapoo fault. Those stresses succeeded in nucleating on the Homestead Valley fault because the two fault traces are close to parallel there; the less parallel orientation of the curved Homestead Valley fault further to the southeast would not have allowed jumping.

[98] When rupture stops at the termination of one fault strand, like on the Kickapoo fault here, the Coulomb stresses radiated to neighboring strands which are either parallel or only slightly misoriented relative to the first strand will increase in an approximately monotonic manner with time, and approach the final static stress distribution associated with the stopped rupture ([Harris and Day, 1993]; also, compare dynamic stressing in Figure 16 with the static results of Figure 6).

[99] Thus, to simply estimate maximum jumpable distances, we have provided an analysis here of the static stress field also. We find that there is a strong sensitivity to the orientation of the target fault, even for misorientations as

small as 5° to 10° (Figure 6). Focusing on parallel faults, we show that the maximum jumpable distance scales as a function of the seismic S ratio, being proportional to $1/(1 + S)^2$. Thus lower S values (i.e., prestress σ_{yx}^0 closer to the static friction strength $-\mu_s\sigma_{yy}^0$) favor jumping a greater distance from a blocked rupture tip.

[100] Low S values also favor transition to supershear propagation speed v_r [Andrews, 1976]. We chose $S = 1.3$ for the simulation presented here, which was large enough to keep v_r sub-Rayleigh on our representation of a part of the Johnson Valley fault and the Kickapoo fault. The jumpable distance was then, nevertheless, still great enough to enable nucleation of propagating rupture on the Homestead Valley fault. While not shown here, we have also done a version of the same analysis with a lower S ratio, which allowed supershear v_r along the Kickapoo fault. As would be expected because the maximum jumpable distance, scaling as $1/(1 + S)^2$, was greater in that case, it too showed a jump of rupture to the Homestead Valley fault. The case presented here provides a more stringent test because of the larger S (i.e., because of the lower shear prestress).

[101] Of course, there will exist a range of sufficiently larger S values for which rupture could not jump from the Kickapoo fault, then under yet lower prestress, to the Homestead Valley fault. In those cases the Landers earthquake could not extend beyond the northern termination of the Kickapoo fault. Such differences in the jumpable distance, depending on prestress along the main fault, might be responsible, among other mechanical reasons, for repeat earthquakes behaving in a variety of ways, sometimes rupturing single fault structures, and sometimes being able to continue, via multiple jumps, to other fault systems.

[102] A phenomenon revealed in our simulations is how adverse curvature of a fault, like for the southern Homestead Valley fault in this modeling, can slow (and surely, sometimes stop) rupture propagation. By adverse curvature, we mean curvature toward the compressional side of a fault, like seen for the southern Homestead Valley fault in Figure 2 [Sowers et al., 1994], just south of the presumed jump site, and Figure 7. Rupture is right lateral and propagates to the SSE on that segment, so the compressional side, toward which the fault curves, is the eastern side. With such curvature, nonuniform slip like that occurring near the rupture tip induces locally increased normal stress, and assuming as we have here that friction strength is proportional to effective normal compression, that locally increases the resistance to slip-weakening failure compared to that which could be estimated based on the fault-normal component of the prestress field. While the curvature significantly slowed, but did not stop, the rupture propagation in our simulations (Figures 17, 19, and 21), it is clear that stronger curvature could stop propagation.

[103] Our analyses here have been based on 2-D modeling. Such modeling has obvious limitations since we address 3-D phenomena. For example, in a 3-D study of the backward branch left by the rupture path in the 1999 Hector Mine earthquake, discussed previously, Oglesby et al. [2003a] found that the branch could not be produced if they allowed, in their simulation, for slip to extend all the way to the Earth's surface along the fault on which rupture nucleated and propagated into the branch junction. They could, however, produce that backward branch if they

assumed that rupture on the first fault was blocked at shallow depths by a strong barrier, thus radiating stress increases to the second fault; that is, in fact, consistent with lack of observed surface slip on the first fault. These results suggest that 3-D dynamic effects may be quite important in determining the rupture path through some complex fault junctions.

[104] Nevertheless, given current computer limitations, it is possible in 2-D modeling, but often not in 3-D, to choose sufficiently small numerical cell sizes as to reasonably resolve the underlying continuum solution (e.g., by having several cells within the region of the fault undergoing slip weakening, a region which contracts in size as rupture speed increases [Rice, 1980; Kame *et al.*, 2003]). Also, the 2-D representation may often be justified when length scales of phenomena modeled are small compared to the thickness of the seismogenic zone, as in this case for the small jump distance involved in the transition from the Kickapoo to Homestead Valley faults.

[105] Such a process as we have investigated, of stopping on one fault strand but thereby radiating stresses to nucleate bilateral propagation on a nearby strand, may provide a general mechanism of backward branching.

[106] **Acknowledgments.** This study was supported at Harvard University by NSF-EAR awards 0105344 and 0440145 and by the Southern California Earthquake Center (SCEC), funded by NSF Cooperative Agreement EAR-0106924 and USGS Cooperative Agreement 02HQAG0008. This is SCEC contribution 780. We are grateful to Nobuki Kame for consultations on the BIE modeling and to David Oglesby, Raul Madariaga, and John Townend for thoughtful reviews.

References

Andrews, D. J. (1976), Rupture velocity of plane strain shear cracks, *J. Geophys. Res.*, **81**, 5679–5687.

Andrews, D. J. (1985), Dynamic plane-strain shear rupture with a slip-weakening friction law calculated by a boundary integral method, *Bull. Seismol. Soc. Am.*, **75**, 1–21.

Aochi, H., and E. Fukuyama (2002), Three-dimensional nonplanar simulation of the 1992 Landers earthquake, *J. Geophys. Res.*, **107**(B2), 2035, doi:10.1029/2000JB000061.

Bouchon, M., and D. Streiff (1997), Propagation of a shear crack on a nonplanar fault: A method of calculation, *Bull. Seismol. Soc. Am.*, **87**, 61–66.

Cochard, A., and R. Madariaga (1994), Dynamic faulting under rate-dependent friction, *Pure Appl. Geophys.*, **142**, 419–445.

Das, S., and K. Aki (1977), A numerical study of two-dimensional spontaneous rupture propagation, *Geophys. J. R. Astron. Soc.*, **50**, 643–668.

Das, S., and B. V. Kostrov (1987), On the numerical boundary integral equation method for three-dimensional dynamic shear crack models, *J. Appl. Mech.*, **54**, 99–104.

Dmowska, R., J. R. Rice, and N. Kame (2002), Fault branching and rupture directivity, *Eos Trans. AGU*, **83**(47), Fall Meet. Suppl., Abstract NG21B-0939.

Felzer, K. R., and G. C. Beroza (1999), Deep structure of a fault discontinuity, *Geophys. Res. Lett.*, **26**, 2121–2124.

Fossum, A. F., and L. B. Freund (1975), Nonuniformly moving shear crack model of a shallow focus earthquake mechanism, *J. Geophys. Res.*, **80**, 3343–3347.

Geubelle, P. H., and J. R. Rice (1995), A spectral method for three-dimensional elastodynamic fracture problems, *J. Mech. Phys. Solids*, **43**, 1791–1824.

Hardebeck, J. L., and E. Hauksson (2001), Crustal stress field in southern California and its implications for fault mechanics, *J. Geophys. Res.*, **106**, 21,859–21,882.

Harris, R. A., and S. M. Day (1993), Dynamics of fault interaction: Parallel strike-slip faults, *J. Geophys. Res.*, **98**, 4461–4472.

Harris, R. A., and S. M. Day (1999), Dynamic 3D simulations of earthquakes on en echelon faults, *Geophys. Res. Lett.*, **26**, 2089–2092.

Harris, R. A., R. J. Archuleta, and S. M. Day (1991), Fault steps and the dynamic rupture process: 2-D numerical simulations of a spontaneously propagating shear fracture, *Geophys. Res. Lett.*, **18**, 893–896.

Harris, R. A., J. F. Dolan, R. Hartleb, and S. M. Day (2002), The 1999 Izmit, Turkey, earthquake: A 3D dynamic stress transfer model of intraearthquake triggering, *Bull. Seismol. Soc. Am.*, **92**, 245–255.

Hauksson, E., L. M. Jones, and K. Hutton (2002), The 1999 M_w 7.1 Hector Mine, California earthquake sequence: Complex conjugate strike-slip faulting, *Bull. Seismol. Soc. Am.*, **92**, 1154–1170.

Ida, Y. (1972), Cohesive force across the tip of a longitudinal-shear crack and Griffith's specific surface energy, *J. Geophys. Res.*, **77**, 3796–3805.

Kame, N., and T. Yamashita (1999), Simulation of the spontaneous growth of a dynamic crack without constraints on the crack tip path, *Geophys. J. Int.*, **139**, 345–358.

Kame, N., J. R. Rice, and R. Dmowska (2003), Effects of pre-stress state and rupture velocity on dynamic fault branching, *J. Geophys. Res.*, **108**(B5), 2265, doi:10.1029/2002JB002189.

Kase, Y., and K. Kuge (1998), Numerical simulation of spontaneous rupture processes on two non-coplanar faults: The effect of geometry on fault interaction, *Geophys. J. Int.*, **135**, 911–922.

Kase, Y., and K. Kuge (2001), Rupture propagation beyond fault discontinuities: significance of fault strike and location, *Geophys. J. Int.*, **147**, 330–342.

Koller, M., M. Bonnet, and R. Madariaga (1992), Modelling of dynamical crack propagation using regularized time-domain boundary integral equation, *Wave Motion*, **16**, 339–366.

Lawn, B. R., and T. R. Wilshaw (1993), *Fracture of Brittle Solids*, 2nd ed., Cambridge Univ. Press, New York.

Li, Y.-G., K. Aki, D. Adams, and A. Hasemi (1994), Seismic guided waves trapped in the fault zone of the Landers, California, earthquake of 1992, *J. Geophys. Res.*, **99**, 11,705–11,722.

Li, Y.-G., J. E. Vidale, S. M. Day, and D. D. Oglesby (2002), Study of the 1999 M 7.1 Hector Mine, California, earthquake fault plane by trapped waves, *Bull. Seismol. Soc. Am.*, **92**, 1318–1332.

Nakata, T., K. Shimazaki, Y. Suzuki, and E. Tsukuda (1998), Fault branching and directivity of rupture propagation (in Japanese), *J. Geogr.*, **107**, 512–528.

Oglesby, D. D., S. M. Day, Y.-G. Li, and J. E. Vidale (2003a), The 1999 Hector Mine earthquake: The dynamics of a branched fault system, *Bull. Seismol. Soc. Am.*, **93**(6), 2459–2476.

Oglesby, D. D., S. M. Day, and D. R. H. O'Connell (2003b), The dynamic and static interaction of two thrust faults: A case study with general implications, *J. Geophys. Res.*, **108**(B10), 2489, doi:10.1029/2002JB002228.

Olsen, K., R. Madariaga, and R. Archuleta (1997), Three dimensional dynamic simulation of the 1992 Landers earthquake, *Science*, **278**, 834–838.

Palmer, A. C., and J. R. Rice (1973), The growth of slip surfaces in the progressive failure of over-consolidated clay, *Proc. R. Soc. London., Ser. A*, **332**, 527–548.

Peyrat, S., K. Olsen, and R. Madariaga (2001), Dynamic modeling of the 1992 Landers earthquake, *J. Geophys. Res.*, **106**(B11), 26,467–26,482.

Poliakov, A. N. B., R. Dmowska, and J. R. Rice (2002), Dynamic shear rupture interactions with fault bends and off-axis secondary faulting, *J. Geophys. Res.*, **107**(B11), 2295, doi:10.1029/2001JB000572.

Rice, J. R. (1968), Mathematical analysis in the mechanics of fracture, in *Fracture, an Advanced Treatise*, vol. II, edited by H. Liebowitz, pp. 191–311, Elsevier, New York.

Rice, J. R. (1980), The mechanics of earthquake rupture, in *Physics of Earth's Interior*, edited by A. M. Dziesiewski, and E. Boschi, *Proc. Int. Sch. Phys. Enrico Fermi*, **78**, 555–649.

Rockwell, T. K., S. Lindvall, M. Herzberg, D. Murbach, T. Dawson, and G. Berger (2000), Paleoseismology of the Johnson Valley, Kickapoo, and Homestead Valley faults: Clustering of earthquakes in the eastern California shear zone, *Bull. Seismol. Soc. Am.*, **90**, 1200–1236.

Rousseau, C.-E., and A. J. Rosakis (2003), On the influence of fault bends on the growth of sub-Rayleigh and intersonic dynamic shear ruptures, *J. Geophys. Res.*, **108**(B9), 2411, doi:10.1029/2002JB002310.

Sowers, J. M., J. R. Unruh, W. R. Lettis, and T. D. Rubin (1994), Relationship of the Kickapoo fault to the Johnson Valley and Homestead Valley Faults, San Bernardino County, California, *Bull. Seismol. Soc. Am.*, **84**, 528–536.

Spotila, J. A., and K. E. Sieh (1995), Geological investigations of a “slip gap” in the surficial ruptures of the 1992 Landers earthquake, southern California, *J. Geophys. Res.*, **100**, 543–559.

Tada, T., and T. Yamashita (1997), Non hypersingular boundary integral equations for two dimensional non-planar crack analysis, *Geophys. J. Int.*, **130**, 269–282.

Yamashita, T., and E. Fukuyama (1996), Apparent critical slip displacement caused by the existence of a fault zone, *Geophys. J. Int.*, **125**, 459–472.

Yamashita, T., and Y. Umehara (1994), Earthquake rupture complexity due to dynamic nucleation and interaction of subsidiary faults, *Pure Appl. Geophys.*, **143**, 89–116.

Zachariasen, J., and K. Sieh (1995), The transfer of slip between two en echelon strike-slip faults: A case study from the 1992 Landers earthquake, southern California, *J. Geophys. Res.*, **100**, 15,281–15,302.

H. S. Bhat, Division of Engineering and Applied Sciences, 327 Pierce Hall, 29 Oxford Street, Harvard University, Cambridge, MA 02138, USA.
(bhat@esag.harvard.edu)

R. Dmowska, Division of Engineering and Applied Sciences, 227 Pierce Hall, 29 Oxford Street, Harvard University, Cambridge, MA 02138, USA.
(dmowska@esag.harvard.edu)

S. Fliss, Laboratoire de Mécanique, Ecole Polytechnique, F-91128 Palaiseau, France. (sonia.fliss@polytechnique.org)

J. R. Rice, Division of Engineering and Applied Sciences, 224 Pierce Hall, 29 Oxford Street, Harvard University, Cambridge, MA 02138, USA.
(rice@esag.harvard.edu)